

Experimentalists are from Mars, Theorists are from Venus

J.L. Nagle (nagle@nevis.columbia.edu)
Columbia University, New York, NY 10027, USA

T. Ullrich (ullrich@bnl.gov)
Brookhaven National Laboratory, Upton, NY 11973, USA

2000/04/29

Abstract. We present a written version of four lectures given at the NATO Advanced Study Institute on “QCD Perspectives on Hot and Dense Matter” in Cargese, Corsica during August, 2001. Over the last year the first exciting results from the Relativistic Heavy Ion Collider (RHIC) and the four experiments BRAHMS, PHENIX, PHOBOS, and STAR have been presented. In these lectures we review the state of RHIC and the experiments and the most exciting current results from Run I which took place in 2000. A complete review is not possible yet with many key results still preliminary or to be measured in Run II, which is currently underway, and thus the emphasis will be on the approach experimentalists have taken to address the fundamental physics issues of the field. We have not attempted to update the RHIC results for this proceedings, but rather present it as a snapshot of what was discussed in the workshop. The field is developing very quickly, and benefits greatly from contact and discussions between the different approaches of experimentalists and theorists.

Keywords: Relativistic Heavy Ions, Quark-Gluon Plasma, Deconfinement, QCD Vacuum

Table of Contents

1	Introduction	2
2	Physics Motivations	2
3	The RHIC Complex	7
4	Experimental Program	11
5	Experimental Techniques	17
6	Physics Results	25
7	Future Measurements	40
8	Summary and Conclusions	48
	References	48



© 2001 Kluwer Academic Publishers. Printed in the Netherlands.

1. Introduction

A good way to proceed in understanding the construction, operation, and physics output from current high-energy heavy ion experiments is to start with the original physics motivations for the experimental program. The Relativistic Heavy Ion Collider project was started in the 1980's with a list of experimental observables for characterizing hot and dense quark and gluonic matter and the expected restoration of approximate chiral symmetry and screening of the long range confining potential of QCD. We give a brief and certainly not complete review of these physics signals. Then we discuss some of the cost, schedule and technology constraints that impacted the design and construction of the RHIC experiments. Finally we present a sample of the first results from the RHIC experimental program from data taken during Run I in the summer of 2000.

2. Physics Motivations

There are three main categories of observables that were originally proposed to study the matter produced in relativistic heavy ion collisions: (1) Thermodynamic properties of the system and indications of a possible first or second order phase transition between hadronic matter and quark-gluon plasma, (2) Signatures for the restoration of approximate chiral symmetry transition, and (3) Signatures for deconfinement and the screening of the long range confining potential between color charges. In the following list, there will be specific channels that need to be observed that essentially specify the types of detectors and experiments necessary.

2.1. THERMODYNAMIC PROPERTIES

One of the most important question in the physics of heavy-ion collisions is thermalization. We want to describe the system in terms of a few thermodynamic properties, otherwise it is not possible to discuss an equation-of-state and a true order to any associated phase transitions. The use of thermodynamic concepts to multi-particle production has a long history. One of the first to apply them in elementary collisions was Hagedorn in the early 1960's [1]. The concept of a *temperature* applies strictly speaking only to systems in at least local thermal equilibrium. Thermalization is normally only thought to occur in the transverse degrees of freedom as reflected in the Lorentz invariant distributions of particles. The measured hadron spectra contain two pieces of information: (i) their normalization, *i.e.* their yields ratios, provide the chemical composition of the fireball at the chemical freeze-out point where the hadron abundances freeze-out and (ii) their transverse momentum spectra

which provides information about thermalization of the momentum distributions and collective flow. The latter is caused by thermodynamic pressure and reflects the integrated equation of state of the fireball matter. It is obvious that the observed particle spectra do not reflect earlier conditions, *i.e.* the hot and dense deconfined phase, where chemical and thermal equilibrium may have been established, since re-scattering erases most traces from the dense phase. Nevertheless, those which are accumulative during the expansion, such as flow, remain. Only direct photons, either real photons or virtual photons that split into lepton pairs, escape the system without re-scattering. Thus these electromagnetic probes yield information on the earliest thermodynamic state which may be dominated by intense quark-quark scattering.

The assumption of a locally thermalized source in chemical equilibrium can be tested by using statistical thermal models to describe the ratios of various emitted particles. This yields a baryon chemical potential μ_B , a strangeness saturation factor γ_s , and the temperature T_{ch} at chemical freeze-out.

So far these models are very successful in describing particle ratios at SPS [2] and now also at RHIC [3]. At RHIC the derived chemical freeze-out temperature are found to be around 175 MeV (165 MeV at SPS) and a baryon chemical potential of around 45 MeV (270 MeV at SPS). It should be stressed that these models assume thermal equilibration but their success together with the large collective flow (radial and elliptic) measured at RHIC is a strong hint that this picture indeed applies.

2.2. CHIRAL SYMMETRY RESTORATION

The phase transition to a quark-gluon plasma is expected to be associated with a strong change in the chiral condensate, often referred to as the restoration of approximate chiral symmetry in relativistic heavy ion collisions is discussed here. Note that although many in the field refer to the restoration of chiral symmetry, the system always breaks chiral symmetry at a small scale due to the non-zero neutral current masses of the up and down quarks.

There are multiple signatures of this transition, including disoriented chiral condensates (DCC), strangeness enhancement, and many others. However, the most promising signature is the in medium modification to the mass and width of the low mass vector mesons. Nature has provided an excellent set of probes in the various low mass vector meson states (ρ , ω , ϕ) whose mass poles and spectra are dynamically determined via the collisions of hadrons or partons. If the hot and dense state produced in heavy ion collisions is composed of nearly massless partons, the $\rho(770)$ meson mass distribution is expected to broaden significantly and shift to lower values of invariant mass. The ρ meson has a lifetime that is $\tau \approx 1 \text{ fm}/c$ and the plasma state created in

RHIC collisions has a lifetime of order $10 \text{ fm}/c$. Thus, the ρ meson is created and decays many times during the entire time evolution of the collision.

The ρ has a dominant decay (nearly 100%) into two pions. However, in this decay mode if the pions suffer re-scattering with other hadrons after the decay, one cannot experimentally reconstruct the ρ meson and information is lost. Given the dense, either partonic or hadronic environment, the probability for pion re-scattering is very large, unless the ρ is created and decays at the latest stages of the time evolution. This time period is often referred to as thermal freeze-out, when elastic collisions cease. Thus a measurement of the ρ as reconstructed via its pion decay channel gives interesting information on the final hadronic stage, but not on the dense phase where chiral symmetry may be restored.

There is an additional decay channel into electron pairs and muon pairs, though with small branching ratios of $4.5 \cdot 10^{-5}$ and $4.6 \cdot 10^{-5}$, respectively. Since the leptons do not interact strongly, after they are produced, they exit the dense system essentially unaffected carrying out crucial information from the core of the system. There is a good analogy in understanding the processes in the center of the sun via neutrino emission, since only neutrinos have a small enough interaction cross-section to pass out of the sun's core largely unaffected. In the case of neutrinos, the more interesting physics of possible neutrino oscillations complicates matters, but that is not a concern in the case of our electron and muons measurements.

One other additional point of interest is that the apparent branching ratio of the ρ into pions and leptons should be modified as observed by experiment. The ρ mesons that decay in medium into pions are not reconstructed, but the ones decaying into electrons are. If one can reconstruct the ρ in both channels one can gauge the number of lifetimes of the ρ the dense medium survives for.

The lifetime of the ρ meson in the rest frame of the plasma depends on its gamma boost in this frame, and thus to study the earliest stages, a measurement of low transverse momentum ρ mesons is desirable. If the ρ decays at rest in the plasma frame, the maximum transverse momentum for the electron or positron is $p_{\perp} \approx 385 \text{ MeV}/c$. These electrons are considered low p_{\perp} and present an experimental challenge to measure for two reasons. First, there are a large number of low momentum charged pions created in these collisions, that results in a charged pion to electron ratio in this p_{\perp} range of 1000 : 1. Thus one needs detectors that can cleanly identify electrons with good momentum resolution, while rejecting the copiously produced pions. The second challenge is that most of the electrons come from pion Dalitz decays ($\pi^0 \rightarrow e^+e^-\gamma$), η Dalitz decays ($\eta \rightarrow e^+e^-\gamma$), and conversions of photons ($\gamma \rightarrow e^+e^-$) mostly resulting from π^0 decays. Ideally one wants to reject these other electrons to enhance the signal contribution from the low mass vector mesons. Conversions are reduced by reducing the amount of

material in the path of produced photons. This restriction is often at odds with the desire to have substantial inner tracking detectors and these needs must be balanced.

The $\phi(1020)$ meson spectral function is also sensitive to in-medium chiral symmetry restoration; however its substantially longer lifetime $\tau \approx 40 \text{ fm}/c$ means that most ϕ decays occur outside the medium. However, measuring the ϕ in its various decay modes (kaon pairs, electron pairs, muon pairs) remains an interesting signal at low transverse momentum.

These low mass vector mesons also decay into muons pairs. These muons have low momentum and are an real experimental challenge to measure as detailed later in these proceedings.

2.3. DECONFINEMENT

There are many signatures that result from the deconfinement of color charges over an extended volume, often referred to as the quark-gluon plasma. Two are detailed in this proceedings: (1) Suppression of heavy quarkonium states and (2) Parton energy loss via gluon emission, also referred to as jet quenching.

2.3.1. *Quarkonium Suppression*

The suppression of heavy quarkonium states was originally proposed by Matsui and Satz [4] in the late 1980's as a signature for color deconfinement. The Debye screening in a QED plasma is a reasonable analogue for the scenario in our QCD plasma. A charm-anticharm ($c\bar{c}$) quark pair produced via gluon fusion in the initial phase of the heavy ion collision can form a J/ψ if the pair has low relative momentum. The total production of such states in proton-proton collisions relative to the total charm production is less than a few percent. If the Debye screening length is of order the same size as the quarkonium state, then the pair is screened. The charm and anticharm quark scatter away from each other and, eventually at the hadronization point, pair with surrounding light quarks and antiquarks to form D mesons. This color screening is displayed in recent lattice QCD calculations described at this workshop in terms of a modification in the linear rise at large distances of the QCD potential. This change in the QCD potential as a function of temperature is shown in Fig. 1.

There are a variety of heavy vector mesons with a large range in binding energy (and associated hadronic size). The J/ψ , χ_c , and ψ' have binding energies of 0.64, 0.20, and 0.05 GeV respectively. The $\Upsilon(1s)$, χ_b , $\Upsilon(2s)$, χ'_b , and $\Upsilon(3s)$ have binding energies of 1.10, 0.67, 0.54, 0.31, 0.20 GeV respectively. Since the suppression of these states is determined by the relative plasma temperature and the binding energy (or by the quarkonium hadronic

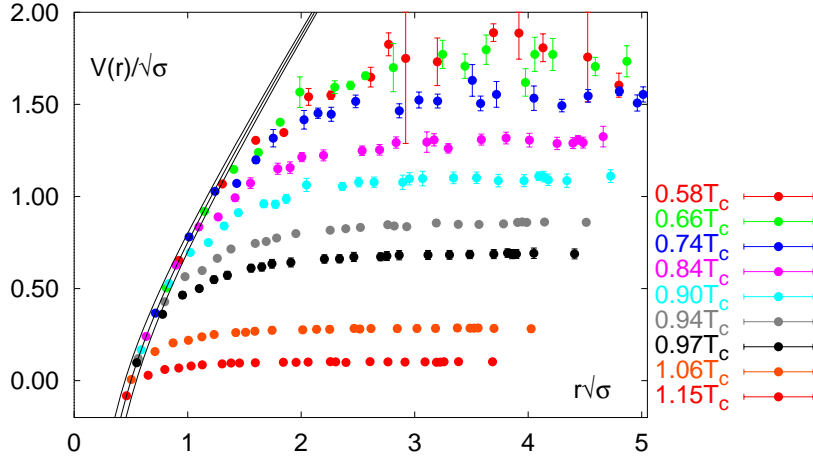


Figure 1. The QCD potential between heavy quarks in shown as a function of $r\sqrt{\sigma}$

size and the Debye screening length), measuring the sequential disappearance of these states acts as a QCD thermometer.

The $J/\psi(1s)$ state decays into almost anything hadronic with a large branching ratio of 87.7%. However, the experimentally accessible decay channels are 5.93% to e^+e^- and 5.88% to $\mu^+\mu^-$. Similar decay channels are available for the ψ' and the Υ states. The accessible decay channel of the χ_c for heavy ion experiments is $\chi_c \rightarrow \gamma + J/\psi$ with a branching ratio $6.6 \cdot 10^{-3}$. Since the decay γ is quite soft, the χ_c represents an experimental challenge.

Similar to the low mass vector mesons there is interest in these states at low transverse momentum, where they reside in the plasma state longer. At rest the J/ψ decays into electrons or muons with a characteristic $p_\perp \approx 1.5$ GeV. A rough rate estimate (good to a factor of 2-3) is that the production of J/ψ is approximately $1 \cdot 10^{-4}$ per proton-proton collision. In a central Au-Au collision, there are of order 800 binary collisions, yielding a J/ψ rate of $8 \cdot 10^{-2}$. The branching ratio to electrons is 5.9% and a typical experimental acceptance is 1%, yielding $4 \cdot 10^{-5}$ J/ψ per Au-Au central collision, and that is assuming no anomalous suppression! Hence, one requires a detector that measures either electron or muon pairs with a high efficiency and a trigger and data acquisition system capable of sampling events at the full RHIC design luminosity. In particular, if one wants to bin the data in terms of x_F , p_\perp , and collision centrality, large statistics are a requirement.

There is a recent proposal for J/ψ enhancement. This scenario assumes copious charm production, and then at the hadronization stage some charm and anticharm quarks may be close in both momentum and configuration space. These $c\bar{c}$ pairs may coalesce to form J/ψ . This late stage production would potentially mask any suppression in the early stages from color screening. There is an easy test of this theory. When RHIC runs at lower energies,

for example $\sqrt{s} = 60$ GeV, instead of the maximum energy of $\sqrt{s} = 200$ GeV, the charm production is lower by a factor of approximately three and the effect of recombination should be reduced substantially. In addition, we expect different p_{\perp} dependence of J/ψ production from original hard processes compared with late stage $c\bar{c}$ coalescence.

2.3.2. Parton Energy Loss

An ideal experiment would be to contain the quark-gluon plasma, and send well calibrated probes through it, and measure the resulting transparency or opacity of the system. There is no experimental way of aiming a third beam of particle at the collision. Therefore any probes of the system must be generated in the collision itself. These probes must have calculable production rates in order to be considered calibrated. An excellent example of such a probe is a hard scattered parton. A parton traversing a color confined medium of hadrons sees a relatively transparent system. However, a parton passing through a hot colored deconfined medium will lose substantial energy via gluon radiation[5, 6].

The source of these partons is from hard scattering processes producing back-to-back parton jets. In a deconfined medium the parton will lose energy before escaping the system and fragmenting into a jet cone of hadrons. The total energy of the initial parton jet is conserved since eventually the radiated gluons will also hadronize. It is likely that the radiated gluons will have a larger angular dispersion than the normally measured jet cone. Thus one might be able to measure a modification in the apparent jet shape. When the parton fragments into hadrons it has less energy, and hence the fragmentation will result in a much reduced energy for the leading hadron. A measurement of high transverse momentum hadrons ($\pi^0, \pi^{+/-}, K^{+/-}, h^{+/-}$) is a strong indicator of the opacity of the medium. An exciting additional observable was mentioned at the workshop in the context of the high p_{\perp} spectra of charm D mesons. There is a reduction in the induced gluon radiation for charm and bottom quarks relative to light quarks due to their slower velocity through the medium.

3. The RHIC Complex

The scope of the RHIC program is to operate a colliding beam facility which allows studies of phenomena in ultra-relativistic heavy-ion collisions and in collisions of polarized protons. The collider is located in the northwest section of the Brookhaven National Laboratory (BNL) in Upton, New York. Its construction began in 1991 and the completion of the complex was accomplished in Spring 2000.

The collider, which consists of two concentric rings of 1740 super-conducting magnets, was constructed in an already existing ring tunnel of ~ 3.8 km circumference. This tunnel was originally constructed for the proposed ISABELLE project. It offers an extraordinary combination of energy, luminosity and polarization. A schematic diagram of the whole RHIC complex, including the various facilities used to produce and pre-accelerate the beams of particles is displayed in Figure 2.

RHIC is able to accelerate and store counter-rotating beams of ions ranging from those of gold to protons at the top energy of 100 GeV/nucleon for gold and 250 GeV for protons. The stored beam lifetime for gold in the energy range of 30 to 100 GeV/nucleon is expected to be approximately 10 hours. The major performance parameters are summarized in Figure 3.

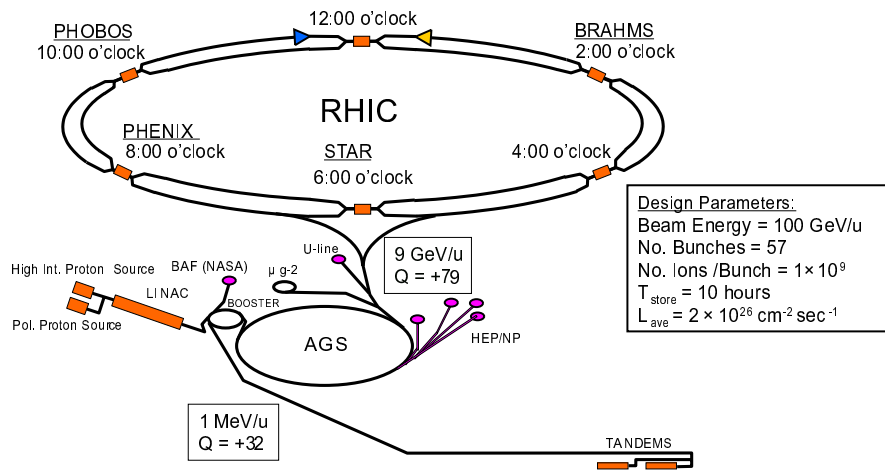


Figure 2. The Relativistic Heavy Ion Collider (RHIC) accelerator complex at Brookhaven National Laboratory. Nuclear beams are accelerated from the tandem Van de Graaff, through the transfer line into the AGS Booster and AGS prior to injection into RHIC. Details of the characteristics of proton and Au beams are also indicated after acceleration in each phase.

The layout of the tunnel and the magnet configuration allow the two rings to intersect at six locations along their circumference. The top kinetic energy is 100+100 GeV/nucleon for gold ions. The operational momentum increases with the charge-to-mass ratio, resulting in kinetic energy of 125 GeV/nucleon for lighter ions and 250 GeV for protons. The collider is able to operate a wide range from injection to top energies. The collider is designed for a Au-Au luminosity of about $2 \cdot 10^{26} \text{ cm}^{-2} \text{ s}^{-1}$ at top energy. This design corresponds to approximately 1400 Au-Au minimum bias collisions per second. The luminosity is energy dependent and decreases approximately proportionally as the operating energy decreases. For lighter ions it is significantly higher reaching $\sim 1 \cdot 10^{31} \text{ cm}^{-2} \text{ s}^{-1}$ for pp collisions. The collider allows collisions of beams of equal ion species all the way down to pp and of

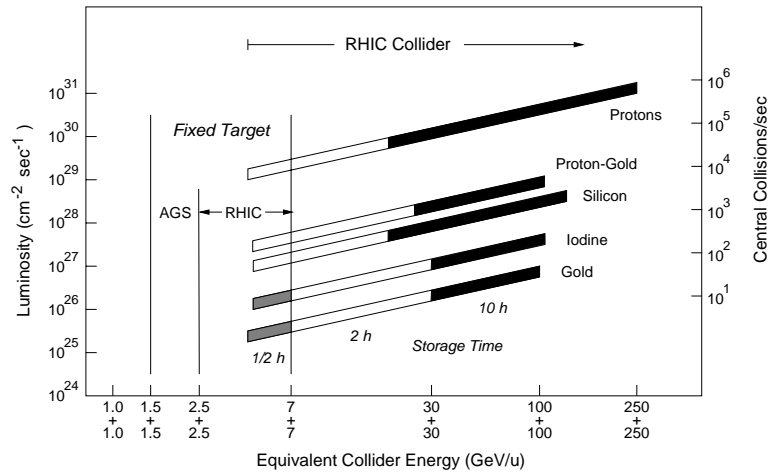


Figure 3. RHC performance parameters.

unequal species such as protons on gold ions. Another unique aspect of RHIC is the ability to collide beams of polarized protons (70-80%) which allows the measurement of the spin structure functions for the sea quarks and gluons.

The first physics run at the Relativistic Heavy Ion Collider (RHIC) took place in the Summer of 2000. For this run beam energies were kept to a moderate 65 A GeV. RHIC attained its goal of ten percent of design luminosity by the end of its first run at the collision center-of-mass energy of $\sqrt{s_{NN}} = 130$ GeV.

In the following we describe briefly the various facilities, depicted in Figure 2, that are part of the large RHIC complex:

Tandem Van de Graaff Completed in 1970, the Tandem Van de Graaff facility was for many years the world's largest electrostatic accelerator facility. It can provide beams of more than 40 different types of ions ranging from hydrogen to uranium. The facility consists of two 15 MV electrostatic accelerators, each about 24 meters long, aligned end-to-end. In the Tandem the atoms are stripped of some of their electrons (e.g. Au to $Q = +32$) and accelerated to a kinetic energy of 1 MeV/nucleon.

Heavy Ion Transfer Line (HITL) To study heavy ion collisions at high energies, a 700 meter-long tunnel and beam transport system called the Heavy Ion Transport Line were completed in 1986, allowing the delivery of heavy ions from the Tandem to the Booster for further acceleration. The HITL makes it possible for the Tandem to serve as the Relativistic Heavy Ion Collider's ions source.

Linear Accelerator (Linac) For the study of pp or pA collisions at the experiments, energetic protons are supplied by an Linear Accelerator (Linac). The Brookhaven Linear Accelerator was designed and built in the late 1960's as a major upgrade to the Alternating Gradient Synchrotron (AGS) complex. The basic components of the Linac include ion sources, a radiofrequency quadrupole pre-injector, and nine accelerator radiofrequency cavities spanning the length of a 150 m tunnel. The Linac is capable of producing up to a 35 milliamper proton beam at energies up to 200 MeV for injection into the AGS Booster.

Booster The Alternating Gradient Synchrotron Booster is less than one quarter the size of the AGS. It is used to preaccelerate particles entering the AGS ring and plays an important role in the operation of the Relativistic Heavy Ion Collider (RHIC) by accepting heavy ions from the Tandem Van de Graaff facility via the Heavy Ion Transfer Line (HITL) and protons from the Linac. It then feeds them to the AGS for further acceleration and delivery to RHIC. After the installation of the HITL in 1986, the AGS was capable of accelerating ions up to silicon with its atomic mass of 28. However, due to its superior vacuum, the Booster makes it possible for the AGS to accelerate and deliver heavy ions up to gold with its atomic mass of 197.

AGS Since 1960, the Alternating Gradient Synchrotron (AGS) has been one of the world's premiere particle accelerators and played a major role in the study of relativistic heavy ion collisions in the last decade. The AGS name is derived from the concept of alternating gradient focusing, in which the field gradients of the accelerator's 240 magnets are successively alternated inward and outward, permitting particles to be propelled and focused in both the horizontal and vertical plane at the same time. Among its other duties, the AGS is now used as an injector for the Relativistic Heavy Ion Collider. For RHIC operation the fully stripped ions are accelerated in the AGS to 9 GeV/nucleon before ejection.

ATR The AGS sends the ions (or protons) down another beamline called the AGS-to-RHIC Transfer Line (ATR). At the end of this line, there's a "fork in the road", where sorting magnets separate the ion bunches. From here, the counter-rotating beams circulate in the RHIC where they are collided at one of four intersecting points.

4. Experimental Program

4.1. LETTERS OF INTENT

In July 1991 there were a set of experimental Letters of Intent that were put forward to an advisory committee. The proposals are listed below, including the lead institution and in parenthesis the physics observable focus.

1. LBL-TPC (inclusive charged hadrons)
2. BNL-TPC (inclusive charged hadrons)
3. TOYKO-TALES (electron pairs, hadrons)
4. SUNY-SB (direct photons)
5. Columbia-OASIS (electron pairs, hadrons, high p_{\perp})
6. ORNL Di-Muon (muon pairs)
7. BNL Forward Angle Spectrometer (hadrons at large rapidity)
8. MIT MARS (hadrons and particle correlations)

The experiments span the range of hadronic, leptonic and photonic capabilities to cover the broad spectrum of physics topics listed above. At the time, only the LBL-TPC proposal was approved and became the STAR experiment. Eventually the MARS proposal evolved into the PHOBOS experiment (note that Phobos is a moon of the planet Mars) and PHENIX (should be spelled Phoenix) rose from the ashes of OASIS, Di-Muon, TALEs and the other lepton focussed experiments.

Eventually there were four approved experiments which have now been constructed and operated during the first year of RHIC running. BRAHMS, PHENIX, PHOBOS and STAR are briefly described below. These experiments have various approaches to study the deconfinement phase transition to the quark gluon plasma. The STAR experiment [7] concentrates on measurements of hadron production over a large solid angle in order to measure single- and multi-particle spectra and to study global observables on an event-by-event basis. The PHENIX experiment [8] focuses on measurements of lepton and photon production and has the capability of measuring hadrons in a limited range of azimuth and pseudo-rapidity. The two smaller experiments BRAHMS (a forward and mid-rapidity hadron spectrometer) [9] and PHOBOS (a compact multiparticle spectrometer) [10] focus on single- and multi-particle spectra. The collaborations, which have constructed these detector systems and which will exploit their physics capabilities, consist of

approximately 900 scientists from over 80 institutions internationally. In addition to colliding heavy ion beams, RHIC will collide polarized protons to study the spin content of the proton [11]. STAR and PHENIX are actively involved in the spin physics program planned for RHIC.

4.2. BRAHMS

The **BR**oad **R**ange **H**adron **M**agnetic **S**pectrometer BRAHMS experiment is designed to measure and identify charged hadrons (π^\pm , K^\pm , (\bar{p})) over a wide range of rapidity and transverse momentum for all beams and energies available at RHIC. Because the conditions and thus the detector requirements at mid-rapidity and forward angles are different, the experiment uses two movable spectrometers for the two regions.

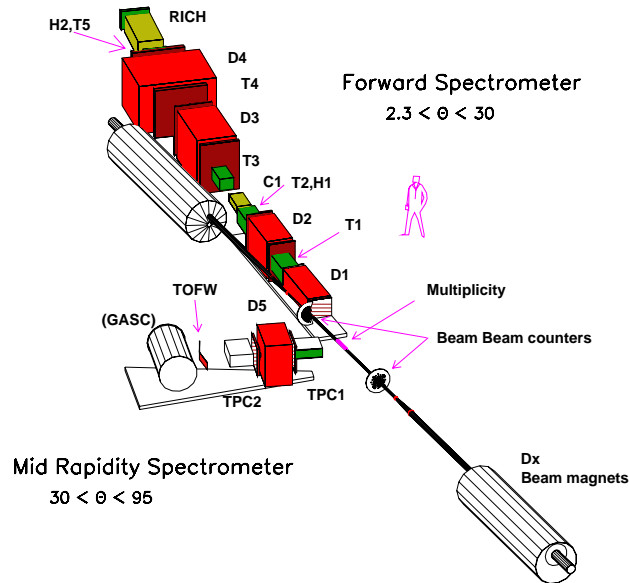


Figure 4. Layout of the BRAHMS detector.

As shown in Figure 4, there is a mid-rapidity spectrometer to cover the pseudo-rapidity range $0 \leq \eta \leq 1.3$ and a forward spectrometer to cover $1.3 \leq \eta \leq 4.0$. The latter employs four dipole magnets, three time projection chambers (TPC), and drift chambers. Particle identification is achieved with time-of-flight hodoscopes, a threshold Cherenkov counter, and one ring-imaging Cherenkov counter (RICH). The solid angle acceptance of the forward arm is 0.8 mstr. The mid-rapidity spectrometer has been designed for charged particle measurements for $p \leq 5 \text{ GeV}/c$. The spectrometer has two TPCs for tracking, a magnet for momentum measurement, and a time-of-flight wall and segmented gas Cherenkov counter (GASC) for particle identi-

fication. It has a solid angle acceptance of 7 mstr. A set of beam counters and a silicon multiplicity array provide the experiment with trigger information and vertex determination.

4.3. PHOBOS

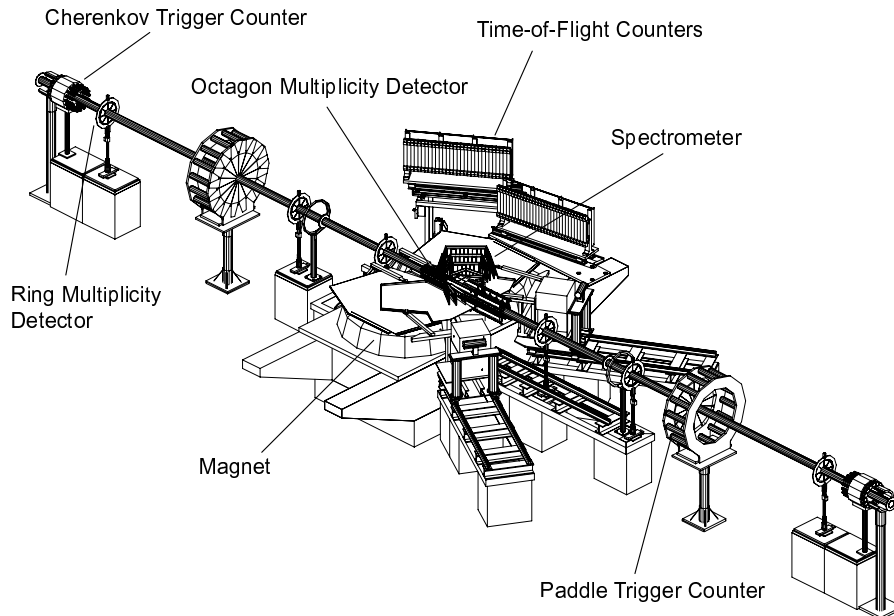


Figure 5. PHOBOS detector setup for the 2000 running period.

The PHOBOS detector is designed to detect as many of the produced particles as possible and to allow a momentum measurement down to very low p_{\perp} . The setup consists of two parts: a multiplicity detector covering almost the entire pseudo-rapidity range of the produced particles and a two arm spectrometer at mid-rapidity. Figure 5 shows the detector, including the spectrometer arms, the multiplicity and vertex array, and the lower half of the magnet.

One aspect of the design is that all detectors are produced using a common technology, namely as silicon pad or strip detectors. The multiplicity detector covers the range $-5.4 < \eta < 5.4$, measuring total charged multiplicity $dN_{\text{ch}}/d\eta$ over almost the entire phase space. For approximately 1% of the produced particles, information on momentum and particle identification will be provided by a two arm spectrometer located on either side of the interaction volume (only one arm was installed for the 2000 run). Each arm covers about 0.4 rad in azimuth and one unit of pseudo-rapidity in the range $0 < \eta < 2$, depending on the interaction vertex, allowing the measurement

of p_{\perp} down to 40 MeV/c. Both detectors are capable of handling the 600 Hz minimum bias rate expected for all collisions at the nominal luminosity.

4.4. PHENIX

The PHENIX experiment is specifically designed to measure electrons, muons, hadrons and photons. The experiment is capable of handling high event rates, up to ten times RHIC design luminosity, in order to sample rare signals such as the J/ψ decaying into muons and electrons, high transverse momentum π^0 's, direct photons, and others. The detector consists of four spectrometer arms. Two central arms have a small angular coverage around central rapidity and consist of a silicon vertex detector, drift chamber, pixel pad chamber, ring imaging Cerenkov counter, a time-expansion chamber, time-of-flight and an electromagnetic calorimeter. These detectors allow for electron identification over a broad range of momenta in order to measure both low mass and high mass vector mesons. Two forward spectrometers are used for the detection of muons. They employ cathode strip chambers in a magnetic field and interleaved layers of Iarocci tubes and steel for muon identification and triggering. The overall layout of the PHENIX detector is shown in Figure 6.

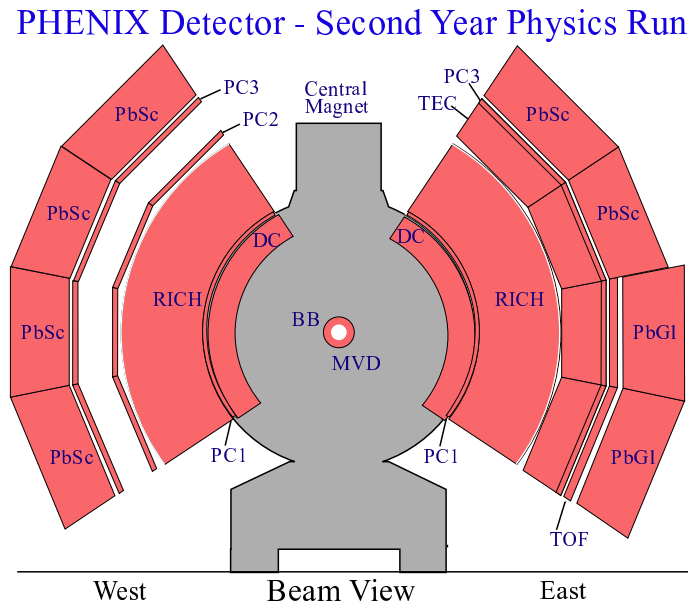


Figure 6. Shown is a beam view of the PHENIX two central spectrometer arms. Their is a axial field magnet in the middle. The detectors from the inner radius out are the multiplicity and vertex detector (MVD), beam-beam counters (BBC), drift chambers (DC), pad chambers (PC1-3), ring imaging cherenkov counter (RICH), time-expansion chamber (TEC), time-of-flight (TOF), and a Lead Glass and Lead Scintillator electro-magnetic calorimeter (PbSc, PbGl).

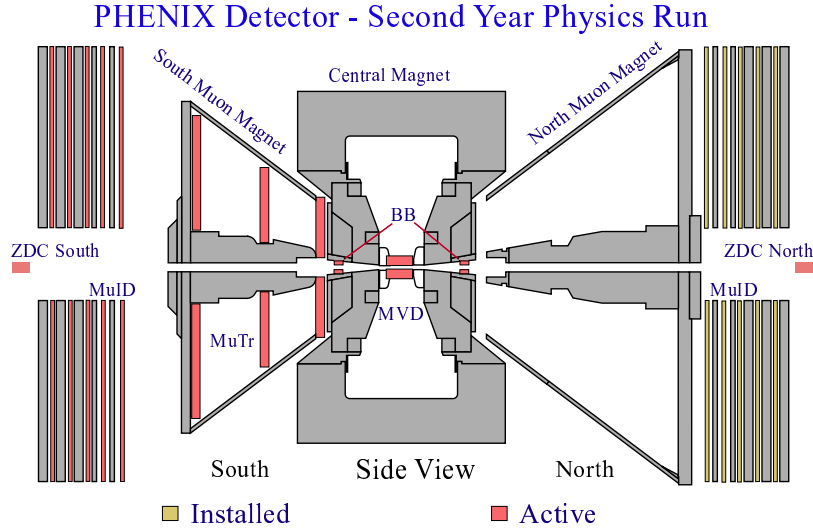


Figure 7. Shown is a side view of the PHENIX detector including the two central spectrometer arms and the two muon spectrometers. The muons systems consist of cathode strip chamber muon trackers (MuTr) and muon identifiers (MuID) interleaved with layers of steel.

One key feature of the PHENIX detector is the high rate capability of the data acquisition system (DAQ) and multi-level trigger architecture. These allow PHENIX to sample physics from RHIC collisions above the design luminosity of the machine. This high rate is crucial for studying rare leptonic, photonic and high p_{\perp} processes.

4.5. STAR

The **Solenoidal Tracker At RHIC (STAR)** is a large acceptance detector capable of tracking charged particles and measuring their momenta in the expected high multiplicity environment. It is also designed for the measurement and correlations of global observables on an event-by-event basis and the study of hard parton scattering processes. The layout of the STAR experiment is shown in Figure 4.5. The initial configuration of STAR in 2000 consists of a large time projection chamber (TPC) covering $|\eta| < 2$, a ring imaging Cherenkov detector covering $|\eta| < 0.3$ and $\Delta\phi = 0.1\pi$, and trigger detectors inside a solenoidal magnet with 0.25 T magnetic field. The solenoid provides a uniform magnetic field of maximum strength 0.5 T for tracking, momentum analysis and particle identification via ionization energy loss measurements in the TPC. Measurements in the TPC were carried out at mid-rapidity with full azimuthal coverage ($\Delta\phi = 2\pi$) and symmetry. A total of 1M minimum bias and 1M central events were recorded during the summer run 2000.

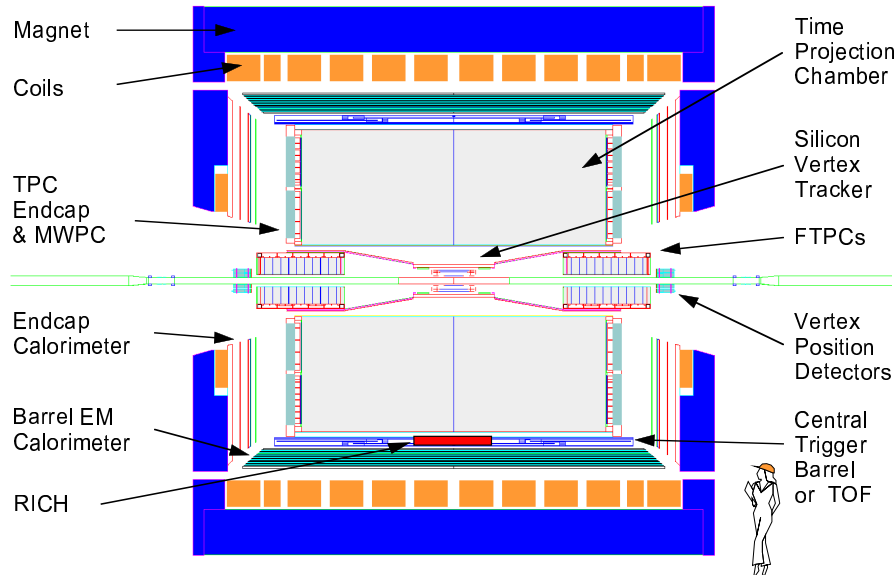


Figure 8. Schematic view of the STAR detector.

Additional tracking detectors will be added for the run in 2001. These are a silicon vertex tracker (SVT) covering $|\eta| < 1$ and two Forward TPCs (FTPC) covering $2.5 < |\eta| < 4$. The electromagnetic calorimeter (EMC) will reach approximately 20% of its eventual $-1 < \eta < 2$ and $\Delta\phi = 2\pi$ coverage and will allow the measurement of high transverse momentum photons and particles. The endcap EMC will be constructed and installed over the next 2 – 3 years.

4.6. RHIC SPIN PROGRAM

The design of both the STAR and PHENIX experiments includes a polarized proton program to conduct studies of the spin structure of the proton. Critical to this measurement is the identification of high transverse momentum photons and leptons. The STAR experiment is phasing in an electromagnetic calorimeter that will be crucial for such observations. In particular the RHIC experiments are ideally suited for measuring the gluon contribution of the proton spin.

5. Experimental Techniques

5.1. TRACKING CHARGED PARTICLES (THE STAR EXAMPLE)

The STAR experiment aims at the observation of hadronic observables and their correlations, global observables on an event-by-event base, and the measurement of hard scattering processes. The physics goals dictate the design of an experiment. Given the physics directions it is easy to summarize the general requirements:

- Soft physics ($100 \text{ MeV}/c < p_{\perp} < 1.5 \text{ GeV}/c$)
 - detection of as many charged particles as possible with high efficiency to provide high statistics for event-by-event observables and fluctuation studies
 - 2π *continuous* azimuthal coverage for reliable event characterization
 - high tracking efficiency as close to the vertex as possible to contain the size of the experiment
 - adequate track length for tracking, momentum measurement and particle identification for a majority of particles
 - good two-track resolution providing a momentum difference resolution of a few MeV/c for HBT studies
 - accurate determination of secondary vertices for detecting strange particles (Λ , Ξ , Ω)
- Hard physics ($> 1.5 \text{ GeV}/c$ and jets)
 - large uniform acceptance to maximize rates and minimize edge effects in jet reconstruction
 - accurate determination of the primary vertex in order to achieve high momentum resolution for primary particles
 - electromagnetic calorimetry combined with tracking and good momentum resolution up to $p_{\perp} = 12 \text{ GeV}/c$ to trigger on jets
 - segmentation of electromagnetic calorimeters which is considerable finer than the typical jet size, *i.e.* jet radius $r = \sqrt{d\eta^2 + d\phi^2} \sim 1$.

The challenge is to find a detector concept which meets all these requirements with minimal costs. The detector of choice to solve the main tracking tasks was a large Time Projection Chamber (TPC) operated in a homogeneous magnetic field for continuous tracking, good momentum resolution and particle identification (PID) for tracks below $1 \text{ GeV}/c$. The requirements not met

by the TPC needed to be covered by more specialized detectors such as a large acceptance electromagnetic calorimeter (hard processes), two Forward-TPCs (coverage of $\eta > 1.7$), and an inner silicon vertex tracker (better primary and secondary vertex measurement). For particle identification of high- p_{\perp} particles detectors a small Ring Imaging Detector (RICH) and a Time-of-Flight (ToF) patch were added. Both detectors are not usable for event-by-event physics due to their small acceptance but allow to extend the PID capabilities for *inclusive* distributions.

The need for an homogeneous field along the beam direction puts a stringent constraint on the design of the whole experiment. Only large solenoidal magnets are able to provide uniform fields of considerable strength (0.5 T). To keep down the costs the magnet cannot be too large which limits significantly the amount of “real estate” (*i.e.* detectors) it can house inside for tracking, PID, and calorimetry. The final magnet has coils with an inner radius of 2.32 m and a yoke radius of 2.87 m. The total length is 6.9 m. Note, that this concept is very different from the design of PHENIX where the axial-field magnet does not, or only weakly, constrain the dimensions of the required detectors.

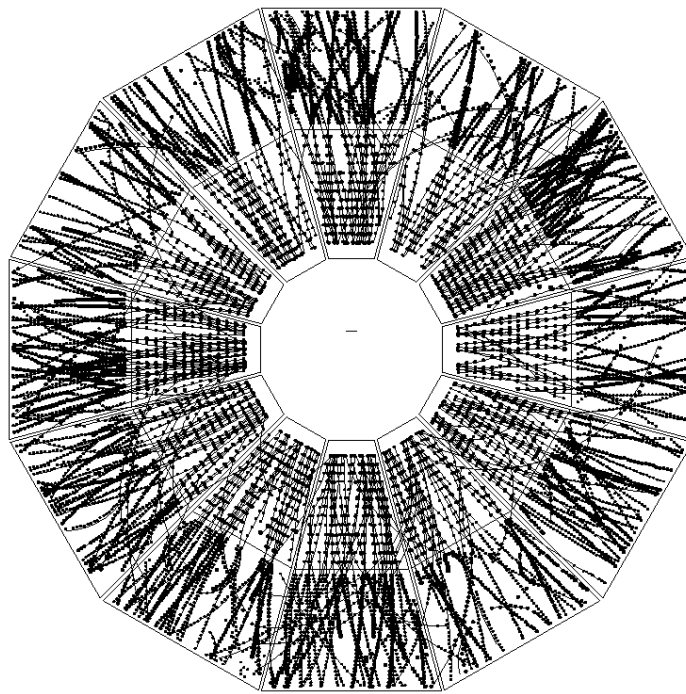


Figure 9. Peripheral Au+Au event recorded in the STAR TPC. Shown is the projection of all hits (points) and reconstructed tracks (solid lines) in the event onto the xy plane perpendicular to the beamline.

In the following we focus on the TPC, STARs main tracking detector, that essentially performs the role of a 3D camera with around 70 million pixel resolution. The TPC is divided into two longitudinal drift regions, each 2.1 m long. Electrons created from track ionization drift in the longitudinal direction, along the TPC electric field lines, to the end-caps of the TPC. Each end-cap is instrumented with 70,000 pads. Each pad reads out 512 time samples. The position of the ionization charge in the readout plane provides the x and y coordinates of a space point along the particle trajectory while the arrival *time* of the charge allows to determine the original z position. The ionization pattern (chain of hits) of a traversing charged particle curved in the magnetic field allows the complete reconstruction of the particle trajectory and its 3-momentum. Fig. 9 shows the xy -projection (front view) of a low multiplicity event recorded in the STAR TPC. Each point represents one reconstructed hit, i.e. the local ionization charge created by one particle. The lines represent the reconstructed trajectories of the particles. Together with the timing information it is possible to also reconstruct the z -position of the hits and such the polar angle of the tracks as shown in Fig. 10. Sophisticated pattern recognition programs perform the task of reconstructing the particle trajectory using the measured positions of the measured hits. This procedure is commonly referred to as “tracking”. In the following we discuss the parameterization used to describe a track in the STAR TPC (and in any other detector with an homogeneous solenoidal field).

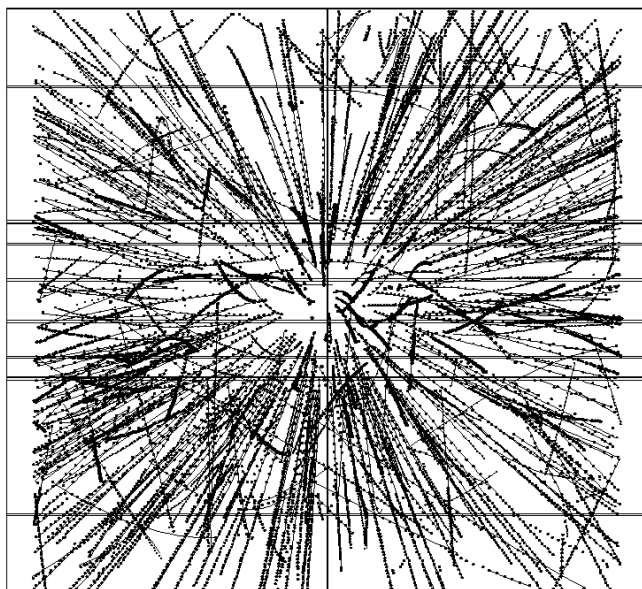


Figure 10. Same event as shown in Fig. 9 but viewed from the side. The beamline runs horizontally from the left to the right.

5.1.1. Track Parameterization Momentum Determination

The trajectory of a charged particle in a static uniform magnetic field with $\vec{B} = (0, 0, B_z)$ is a helix. In principle five parameters are needed to define a helix. From the various possible parameterizations we describe here the version which is most suited for the geometry of a collider experiment and therefore used in STAR.

This parameterization describes the helix in Cartesian coordinates, where x , y and z are expressed as functions of the track length s .

$$x(s) = x_0 + \frac{1}{\kappa} [\cos(\Phi_0 + h s \kappa \cos \lambda) - \cos \Phi_0] \quad (1)$$

$$y(s) = y_0 + \frac{1}{\kappa} [\sin(\Phi_0 + h s \kappa \cos \lambda) - \sin \Phi_0] \quad (2)$$

$$z(s) = z_0 + s \sin \lambda \quad (3)$$

where: \mathbf{s} is the path length along the helix

$\mathbf{x}_0, \mathbf{y}_0, \mathbf{z}_0$ is the starting point at $s = s_0 = 0$

λ is the dip angle

κ is the curvature, i.e. $\kappa = 1/R$

\mathbf{B} is the z component of the homogeneous magnetic field ($B = (0, 0, B_z)$)

\mathbf{q} is charge of the particle in units of positron charge

\mathbf{h} is the sense of rotation of the projected helix in the xy -plane, i.e. $h = -\text{sign}(qB) = \pm 1$

Φ_0 is the azimuth angle of the starting point (in cylindrical coordinates) with respect to the helix axis ($\Phi_0 = \Psi - h\pi/2$)

Ψ is the $\arctan(dy/dx)_{s=0}$, i.e. the azimuthal angle of the track direction at the starting point.

The meaning of the different parameters is visualized in Fig. 11.

The circle fit in the xy -plane gives the center of the fitted circle (x_c, y_c) and the curvature $\kappa = 1/R$ while the linear fit gives z_0 and $\tan \lambda$. The phase of the helix (see Fig. 11) is defined as follows:

$$\Phi_0 = \arctan \left(\frac{y_0 - y_c}{x_0 - x_c} \right) \quad (4)$$

The reference point (x_0, y_0) is then calculated as follows:

$$x_0 = x_c + \frac{\cos \Phi_0}{\kappa} \quad (5)$$

$$y_0 = y_c + \frac{\sin \Phi_0}{\kappa} \quad (6)$$

and the helix parameters can be evaluated as:

$$\Psi = \Phi_0 + h\pi/2 \quad (7)$$

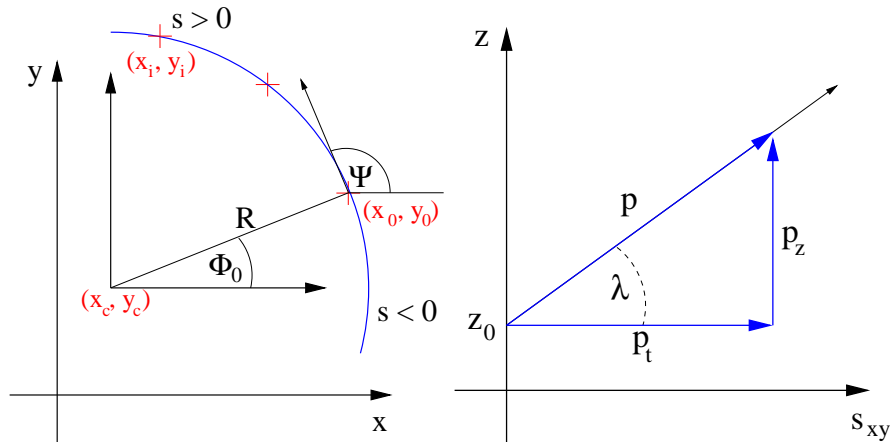


Figure 11. Helix parameterization: shown on the left is the projection of a helix on the xy plane. The crosses mark possible data points. The right plot depicts the projection of a helix on the sz plane. For the meaning of the various parameters see text.

$$p_{\perp} = c q B / \kappa \quad (8)$$

$$p_z = p_{\perp} \tan \lambda \quad (9)$$

$$p = \sqrt{p_{\perp}^2 + p_z^2} \quad (10)$$

where κ is the curvature in [m^{-1}], B the value of the magnetic field in [Tesla], c the speed of light in [m/ns] (≈ 0.3) and p_{\perp} and p_z are the transverse and longitudinal momentum in [GeV/c].

Once the track momenta and parameters are determined, one can use the above parameterization to extrapolate the TPC tracks to other detectors, e.g. outwards to the electromagnetic calorimeter or RICH detector, or inwards to the silicon vertex tracker (SVT). Once the referring hits are found they are added to the track and the parameters are re-evaluated. The charges of all hits along a track can be used to calculate its energy loss (dE/dx) and together with its known momentum can be used to determine the particle mass.

5.2. ELECTRON IDENTIFICATION (THE PHENIX EXAMPLE)

As we have seen in the physics motivation section, there are many reasons to measure electrons over a broad range in transverse momentum. In the original Letters of Intent there were many different proposals for detector technologies for measuring electrons, and many of these capabilities were combined into the PHENIX experiment. The PHENIX experiment has two central spectrometer arms each covering 90 degrees in ϕ and $|\eta| < 0.35$.

Electrons and also charged hadrons that are produced near mid-rapidity are bent in an axial magnetic field over a radial distance of approximately

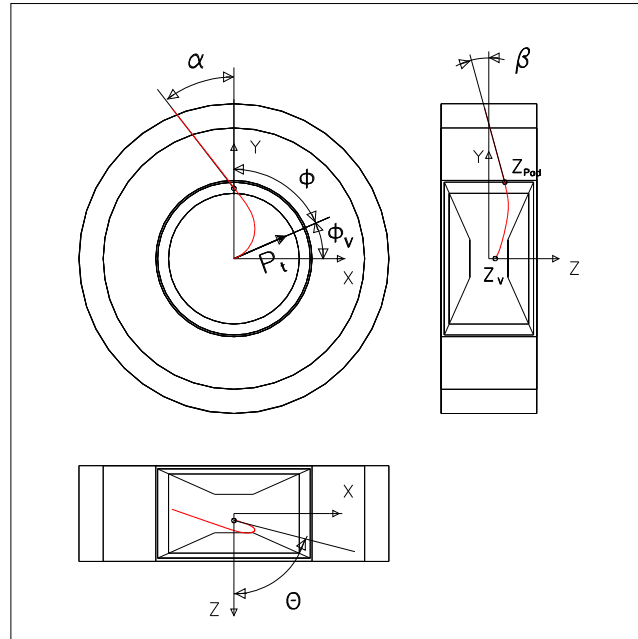


Figure 12. A schematic diagram of the PHENIX central spectrometer magnetic reconstruction technique is shown.

two meters after which the aperture is relatively field free. There is a large aperture drift chamber that measures the projective trajectory of the charged particle tracks in the field free region with multiple wire layers oriented in the x direction (giving maximum resolution in the bend plane of the field) and also in u and v direction (stereo planes for pattern recognition). The drift chamber is augmented by a series of moderate resolution pad chambers, which yield three dimensional space point along the particle's track and aid significantly in pattern recognition and non-vertex background rejection. As shown in Figure 12 the particle track is characterized by an angle (α) in the bend plane of the magnetic field. From this vector and the assumption that the track originated at the Au-Au collision vertex, the rigidity of the track is determined. The rigidity is the momentum divided by the particle charge, and with the assumption of a $Z = \pm 1$ particle, the momentum is known.

Typically the momentum resolution has two components as shown below.

$$\delta p/p = (\approx 1\%) + (\approx 1\%) \times p[\text{GeV}/c] \quad (11)$$

The first term, typically of order 1% is due to the multiple scattering of the charge particle in material before and in the tracking devices. The second term which scales with the particle's momentum is related to the finite spatial resolution of the detector. The PHENIX detector has been designed with a minimum of inner region material including a Beryllium beam pipe, which

has a low Z value to minimize multiple scattering while maintaining integrity for the vacuum. All four experiments at RHIC have Be beam-pipes in the interaction region. The PHENIX design resolution from the drift chamber is of order 0.5% at $p_{\perp} \approx 0.2$ GeV and increases linearly with p_{\perp} above 0.7 GeV. There is a great deal of work involved in calibrations and wire alignment to achieve these resolution values.

It is notable that PHENIX uses an axial field magnet for the central spectrometers as opposed to a solenoidal field. There are substantial advantages and disadvantages to this choice. One major consideration is that if the entire experiment is contained inside a large solenoid, as in the STAR configuration, the magnetic field is present throughout the volume. This is advantageous for the large volume Time Projection Chamber (TPC) of STAR where they can observe the curvature of the charged particle tracks. However, the cost of these magnets increases steeply as one increased the desired outer radius. PHENIX for the purposes of hadron particle identification wanted to have a Time-of-Flight scintillator wall approximately 5 meters from the interaction vertex and for electron and photon identification a good energy resolution and high granularity electromagnetic calorimeter behind that. In keeping within the experimental budget it would not have been possible to have a solenoidal magnet with an outer radius greater than 5.5 meters. The ALICE experiment being built for the CERN-LHC program is fortunate to be able to re-use the very large solenoid from the L3 experiment at LEP. One disadvantage of the PHENIX choice is that the pole tips of the axial field magnet are close to the interaction point and create substantial “shine”, particles scattering off the poles into the detector aperture. The overall choice for the field configuration is an important starting point for many detector designs.

Now that we have characterized the particle’s momentum vector, we must discriminate all of the charged pions from our interesting electrons. The first detector in PHENIX that is employed is a Ring Imaging Cherenkov detector (RICH). It is a large gas volume detector with a thin mirror plane for reflecting Cherenkov light onto an array of photo-multiplier tubes (PMT) that are situated off to the side of the spectrometer acceptance. The radiator gas used is either ethane with an index of refraction $n=1.00082$ or methane with $n=1.00044$. Requiring more than three PMT hits yields almost 100% efficiency for electrons and rejects pions with $p_{\perp} \approx < 4$ GeV at the level of $< 10^3$ in a single track environment. The detector, requiring only three PMT’s, does not reconstruct a ring radius for further particle characterization, but rather is used as a threshold detector only.

In a multiple track collisions (remember of order 5000 charged particles are being produced) one can incorrectly match a track to a RICH signal. Further electron identification is provided by the electromagnetic calorimeter (EMCal). The calorimeter is composed of both Lead Scintillator (PbSc) and Lead Glass (PbGl) modules, with the later being originally used in the WA98

experiment at the CERN-SPS heavy ion program. The calorimeter has a radiation length of $\approx 18X_0$ and $\approx 16X_0$ for the PbSc and PbGl respectively, but does not fully interact and contain hadronic showers. Thus, an electron or photon incident on the calorimeter deposits most of its energy, while a hadron (eg. charged pion) has a large probability to pass through the module depositing a small dE/dx minimum ionizing radiation energy. Even when the pion suffers an inelastic collision in the calorimeter, only a fraction of its energy is contained and measured in the PMT at the back of the module. The excellent energy resolution $\approx 5 - 8\%/\sqrt{E(\text{GeV})}$ and high granularity give precise electron identification and pion rejection by requiring the energy match the measured momentum ($E/p \approx 1$). However, the background rejection degrades when the particle momentum is low and hadronic showers have a higher probability to match the measured momentum.

Therefore, an additional detector is necessary to help identify low p_\perp electrons for the crucial low mass vector meson physics. For this purpose, PHENIX uses a Time Expansion Chamber (TEC) that samples energy loss in a gas radiator. The TEC determines the particle species using dE/dx information. It has a rejection of $e/\pi \approx 5\%$ for particles with a momentum $p = 500$ MeV/ c with P10 gas and 2% with Xe gas, which is much more expensive. It is the combination of all these detectors that allow for efficient electron measurements with a minimum of pion contamination. Thus, the challenge of electron identification over a broad range in p_\perp is met.

5.3. MUON IDENTIFICATION (THE PHENIX EXAMPLE)

Direct muons and hadrons decaying into muons require a rather different experimental approach to measuring electrons, photons and other hadrons. Muons interact with a low cross section in material, and are easiest to identify by placing steel or other material in the particle path and removing all other particles through interaction. Then a detector placed after the steel should measure a clean muon sample.

However, the muons must have a large enough energy to penetrate the steel without stopping due to ionization energy loss dE/dx . In the central rapidity region at a collider, the muons from low p_\perp J/ψ decays make it impossible to have enough steel to range out other hadrons effectively, while allowing the muons to pass through. In particle experiments that focus on high p_\perp muons, the detector can consist of a similar one to that described above for electrons. After the calorimeter, one can have some steel absorber (often the return in the magnet steel) and then have a muon identifier detector outside of that. This design does not work well for heavy ion physics. First, it restricts the measurable p_\perp range at too high a value and also has a large background from low p_\perp pions decaying into muons.

Another option is to measure muons in forward rapidity where they have a substantial momentum in the longitudinal direction. PHENIX measures muons in the forward and backward pseudo-rapidity regions (at angles of 10-35 degrees from the beam line). The detector consists of a brass and steel absorber to range out hadrons followed by a cathode strip chamber muon tracking device that measures the particle's bend in a magnetic field. There is a delicate balance in the amount and type of absorber material used. Too much material and the multiple scattering reduces the resolution which is important for cleanly separating states such as J/ψ and ψ' , and too little material in which case the particle occupancy in the tracking device is too large. After the muon tracking device there is more steel absorber with Larocci tube muon identifiers interspersed. The coverage is from $1.1 \leq |\eta| \leq 2.4$ and the muons must have $E \geq 2.1$ GeV in order to penetrate the absorber material. The identifier detectors also provide the necessary trigger information to sample the muons from the high luminosity RHIC collisions.

The most substantial background in measuring J/ψ and D mesons are muons from pions and kaons that decay before they hit the brass nose-cone absorbers. There is a competing requirement in PHENIX in that one wants the absorber as close to the interaction vertex as possible to reduce this decay contribution, but they need to be far enough apart for there to be a good acceptance for electrons, hadrons and photons in the two central arm spectrometers. There are many benefits to the comprehensive design of PHENIX, but there are definite drawbacks as well. Of the two muon arms, the south muon arm was completed for running in Run II at RHIC, and the north arm will be complete for Run III.

6. Physics Results

In this chapter we present the physics results from the Run I data and a preview of expected results from Run II.

6.1. GLOBAL OBSERVABLES

The first result with a measurement from all four RHIC experiments is the charged particle multiplicity [12, 13, 14, 15]. The four experiments' results for central (small impact parameter) collisions are in excellent agreement and are shown in Figure 13. The multiplicity rises more sharply as a function of center-of-mass energy in heavy ion collisions than in $p+p$ and $p+\bar{p}$ collisions, which is attributed to the increased probability for hard parton scattering in the thick nuclear target seen by each parton.

We expect the charge particle yield to increase for collisions of larger nuclei. However, at low x values, the high density of gluons may in fact

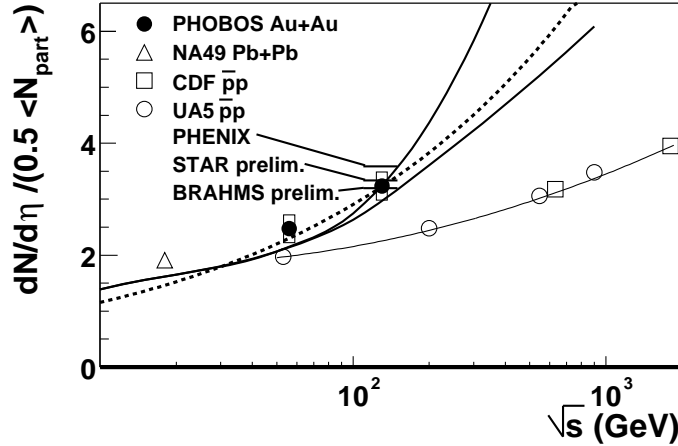


Figure 13. Charged particle multiplicity measurement from all four RHIC experiments is shown for Au-Au collisions at $\sqrt{s_{NN}} = 130$ GeV. Also shown are data for $p + p$ and $p + \bar{p}$ collisions. A model of heavy ion collisions HIJING is shown for comparison.

saturate due to gluon fusion processes. The contribution to the yield from hard processes should exhibit point-like scaling (scaling with the number of binary collisions) and would thus scale as $A^{4/3}$. However, parton saturation depends upon the nuclear size and would limit the growth of the number of produced partons as $A^{1/3}$. If present, this initial parton saturation would limit the hard process contribution to the total charged particle multiplicity.

Only one nuclear species (Au) was accelerated in Run I at RHIC. Thus, rather than changing the mass number A directly we control the collision volume by varying the centrality or the number of participating nucleons for Au-Au collisions. Shown in Figure 14 are the published results from the PHENIX [13] and PHOBOS [16] experiments for the number of charged particles per participant nucleon pair as a function of the number of participating nucleons. The number of participating nucleons is determined in a slightly different manner by the different experiments. However, the general method is to calibrate the number of spectator nucleons ($= 2 \times A -$ participant nucleons) using a measurement of spectator neutrons in a set of zero degree calorimeters that are common to all experiments. By correlating the number of forward neutrons to the number of charged particles produced in the large pseudo-rapidity region, the event geometry can be understood.

In Figure 14 one can also see theory comparisons that indicate that a model including parton saturation (EKRT [17]) fails to agree with the more peripheral data. Results from the HIJING model [18] are also shown which does not include parton saturation and thus has a more continuous rise in the particle multiplicity. Since saturation phenomena are only likely to have observable consequences for large collision volumes, it is not possible with

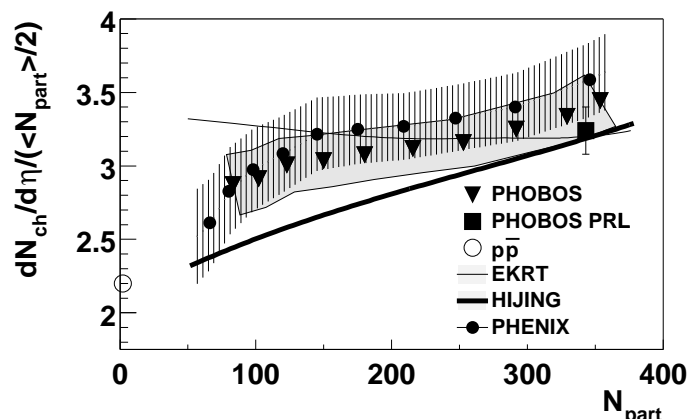


Figure 14. PHENIX and PHOBOS results for $dN_{ch}/d\eta|_{\eta=0}/\frac{1}{2}N_{part}$ as a function of N_{part} . The hashed and solid bands indicate the systematic errors for the two experimental results. The data point for $p\bar{p}$ with two participants is shown for comparison. Also theoretical predictions from the HIJING and EKRT models are shown.

present systematics to rule out the saturation picture for the most central collisions.

In order to better test the saturation picture lighter ion, smaller A , collisions will be studied in Run II. In addition, heavy flavor (charm and bottom) and Drell-Yan production should be a sensitive probe to the initial parton density. Another proposal is that by varying the collision energy and keeping the nuclear geometry the same one can get a better handle on systematics and test scenarios dependent on the coupling constant and the saturation scale. The physics of parton saturation and color glass condensates is at the forefront of theoretical development in the field. Many recent developments were discussed in this workshop and will be described in other contributions.

In addition to the initial parton density, the energy density is of great interest. There are published results estimating the initial thermalized energy density achieved in these collisions. Bjorken originally derived a formula, shown in Eqn. 12, relating the measured transverse energy per unit rapidity to the thermal energy density [19].

$$\epsilon_{Bj} = \frac{1}{\pi R^2} \frac{1}{c\tau} \frac{dE_{\perp}}{dy} \quad (12)$$

It should be noted that there is a trivial factor of two error in the original reference that is corrected here. This formulation assumes a boost invariant expanding cylinder of dense nuclear matter and a thermalization time τ . There are two important assumptions in this particular formulation. The first is the boost invariant nature of the collision. There are recent preliminary measurements from STAR and PHOBOS that indicate the distribution of particles is relatively flat over ± 2 units of pseudo-rapidity. However, shown

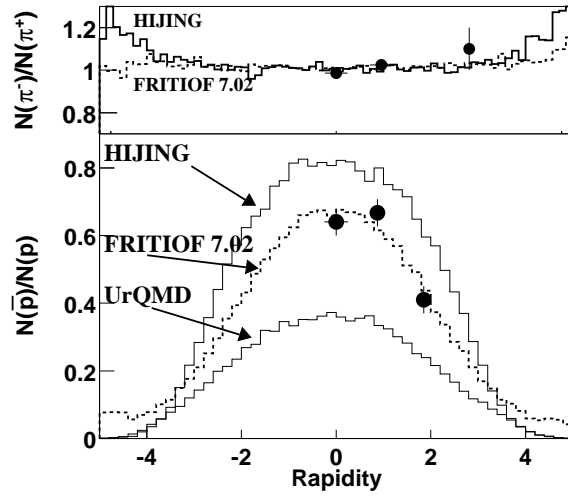


Figure 15. Plotted is the π^-/π^+ and \bar{p}/p ratio as a function of rapidity from the BRAHMS experiment for central collisions.

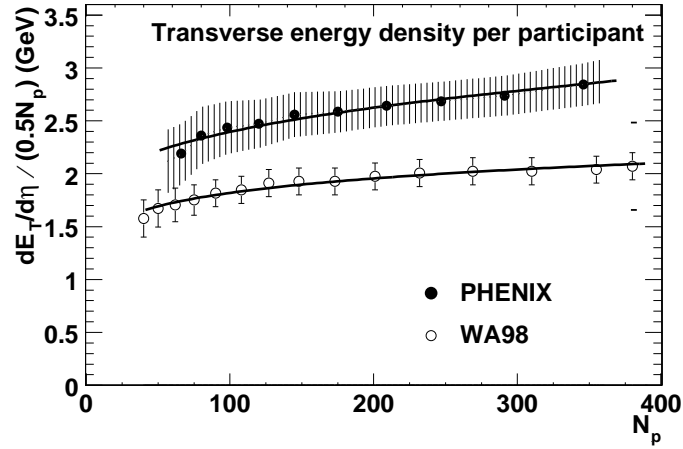


Figure 16. The PHENIX experiment result is shown for $dE_{\perp}/d\eta/(0.5N_p)$ at $\eta = 0$ as a function of the number of participating nucleons. Also shown in the result from experiment WA98 at the lower energy CERN-SPS.

in Figure 15 is the measured distribution of \bar{p}/p from the BRAHMS experiment [20]. This indicates the the system is already changing at $y \approx 2$, though it is not clear that this is enough to invalidate the energy density formulation. The second question is what is the relevant thermalization time τ .

The PHENIX experiment has published [21] the transverse energy distribution for minimum bias Au-Au collisions. For the 5% most central events, the extracted transverse energy $\langle dE_{\perp}/d\eta \rangle|_{\eta=0} = 503 \pm 2$ GeV. Shown in Figure 16 is $dE_{\perp}/d\eta/(0.5N_p)$ versus the number of participating nucleons. One sees a similar increase in transverse energy as was seen in the charged particle multiplicity yield.

The canonical thermalization time used in most calculations is $\tau = 1$ fm/c, that yields an energy density of 4.6 GeV/fm³, which is 60% larger than measured at the CERN-SPS. In addition, it is believed that the density is substantially higher due to the potentially much shorter thermalization time in the higher parton density environment. If one achieves gluon saturation the formation time is of order 0.2 fm/c and gives an estimated energy density of 23.0 GeV/fm³. There are even estimates of over 50 GeV/fm³, but they assume a very large drop in the final measured transverse energy due to work done in the longitudinal expansion of the system. All of these estimates are above the energy density of order 0.6 – 1.8 GeV/fm³ corresponding to the phase transition temperature 150 – 200 MeV.

6.2. ELLIPTIC FLOW

The azimuthal anisotropy of the transverse momentum distribution for non-central collisions is thought to be sensitive to the early evolution of the system. The second Fourier coefficient of this anisotropy, v_2 , is called elliptic flow [22]. It is an important observable since it is sensitive to the re-scattering of the constituents in the created hot and dense matter. This re-scattering converts the initial spatial anisotropy, due to the almond shape of the overlap region of non-central collisions, into momentum anisotropy. The spatial anisotropy is largest early in the evolution of the collision, but as the system expands and becomes more spherical, this driving force quenches itself. Therefore, the magnitude of the observed elliptic flow reflects the extent of the re-scattering at early time [23]. The time evolution of the transverse energy density profile is schematically depicted in Figure 17 where the solid lines represent surfaces of constant energy density. The pressure in the system is highest in direction of the reaction plane (largest energy density gradient) which causes the elliptic anisotropy.

Elliptic flow in ultra-relativistic nuclear collisions was discussed as early as 1992 [24] and has been studied intensively in recent years at AGS [25, 26], SPS [27, 28, 29] and now at RHIC [30] energies. The studies at the top AGS energy and at SPS energies have found that elliptic flow at these energies is in the plane defined by the beam direction and the impact parameter, $v_2 > 0$, as expected from most models.

The STAR detector is especially suited to study elliptic flow due to its azimuthal symmetry, large coverage, and its capability of tracking charged

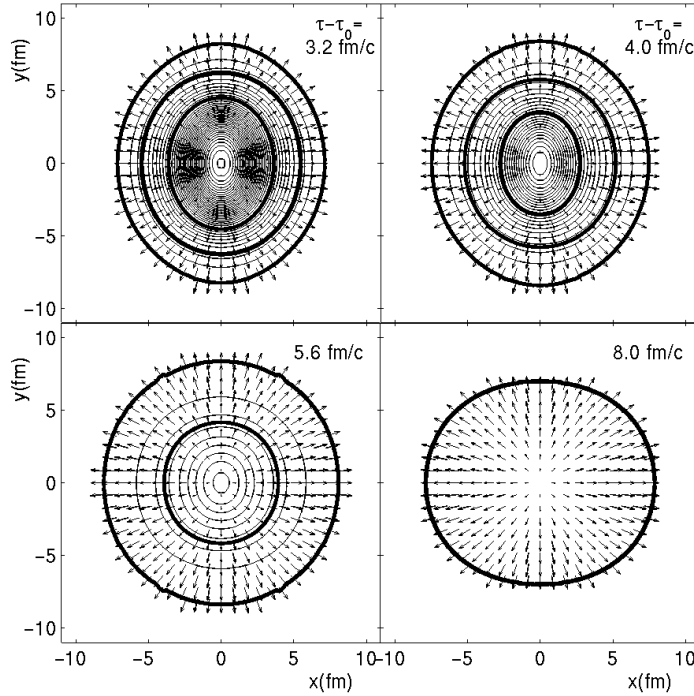


Figure 17. Schematic view of a evolution of the transverse energy density profile (indicated by constant energy density contours spaced by) and of the flow velocity field (indicated by arrows) for Pb+Pb collisions at impact parameter $b=7.0$ fm. The four panels show snapshots at times $\tau - \tau_0 = 3.2, 4.0, 5.6,$ and 8.0 fm/c. At these times the maximal energy densities in the center are $5.63, 3.62, 1.31$ and 0.21 GeV/fm³, respectively. The figure is taken from [32].

particles down to very low p_{\perp} . Even in peripheral events there are sufficient tracks available to divide the event in two 'subevents' of which one is used to measure, or better estimate, the event plane and the other to correlate the particles in it in order to derive v_2 . While BRAHMS is not able to study elliptic flow because of its small acceptance, PHOBOS has some capabilities to measure v_2 but only integrated over all p_{\perp} . Because of its restricted azimuthal coverage the PHENIX collaboration follows a different approach to reconstruct v_2 by studying the $\Delta\phi$ correlation between particles thus circumventing the event plane determination. However, work is still in progress and in the following we concentrate on the more direct event plane method used in STAR.

The flow analysis method involves the calculation of the event plane angle, which is an experimental estimator of the real reaction-plane angle. The second harmonic event plane angle, Ψ_2 , is calculated for two sub-events, which are independent subsets of all tracks in each event. Figure 18 shows the results for the correlation between the sub-events for the first and second

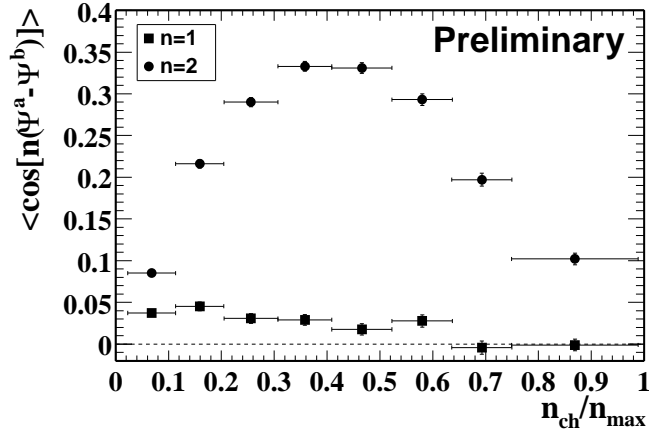


Figure 18. The correlation between the event plane angles determined for two independent sub-events. The correlation is calculated for the first harmonic ($n=1$) and the second harmonic ($n=2$).

harmonic as a function of centrality [30]. The peaked shape of the centrality dependence of $\langle \cos[2(\Psi_a - \Psi_b)] \rangle$ is a signature of anisotropic flow. However, the correlation between the sub-events may not be due entirely to anisotropic flow. To estimate the magnitude of non-flow effects one can use the sub-events in three different ways:

1. Assigning particles with pseudo-rapidity $\eta < 0 + \epsilon$ to one sub-event and particles with $\eta > 0 + \epsilon$ to the other. Short range correlations, such as Bose-Einstein or Coulomb, are to a large extent eliminated by the 2ϵ “gap” between the two sub-events.
2. Dividing randomly all particles into two sub-events, sensitive to all non-flow effects.
3. Assigning positive particles to one sub-event and negative particles to the other, allowing an estimation of the contribution from resonance decays.

Studies have shown that the results from all three methods are for the central and mid-peripheral events very similar. For the most peripheral events the results vary among the methods by about 0.005. Not all non-flow contributions might be known and the effects of others, such as jets, are difficult to estimate because of their long-range correlation. In order to estimate the systematic uncertainty due to the effects of jets, one can assume that jets contribute at the same level to both the first and second order correlations. Taking the maximum observed positive first order correlation, as being completely due to non-flow will reduce the calculated v_2 values.

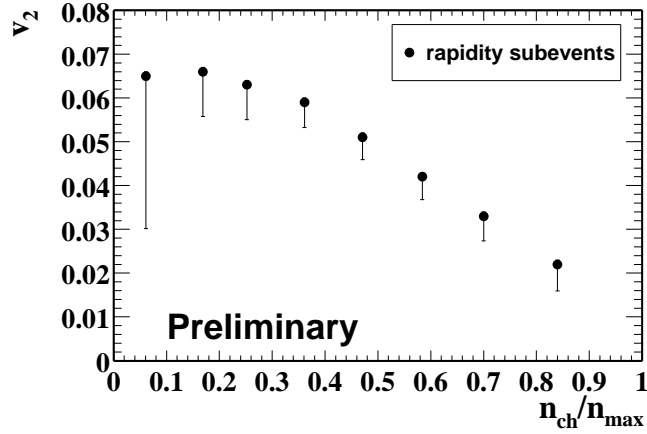


Figure 19. The integrated elliptic flow signal, v_2 , with the estimated systematic uncertainties as measured by STAR.

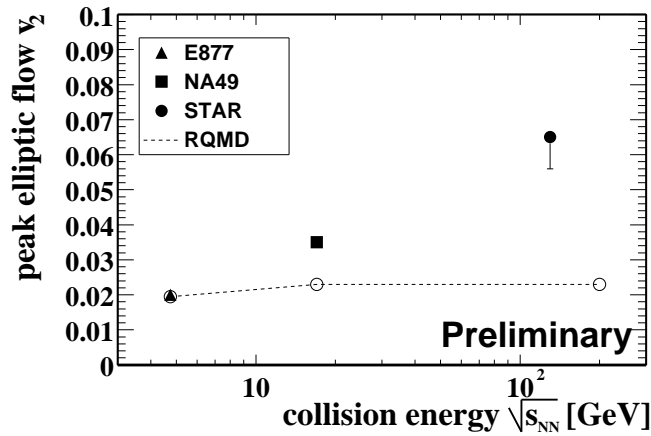


Figure 20. Excitation function of v_2 from top AGS to RHIC energies.

Figure 19 shows the final v_2 integrated over all p_{\perp} as a function of centrality. The statistical uncertainties are smaller than the markers and the uncertainties shown are the systematic uncertainties due to this estimated non-flow effect.

Figure 20 shows the maximum v_2 value as a function of collision energy. It rises monotonically from about 0.02 at the top AGS energy [25], 0.035 at the SPS [28] to about 0.06 at RHIC energies [30]. This increasing magnitude of the integrated elliptic flow indicates that the degree of thermalization,

which is associated with the amount of re-scattering, is higher at the higher beam energies. However, interpretation of the excitation function has to be done with care. The v_2 values used here are the maximum values as a function of centrality for each energy. The centrality where v_2 peaks can change as a function of beam energy, indicating different physics [31].

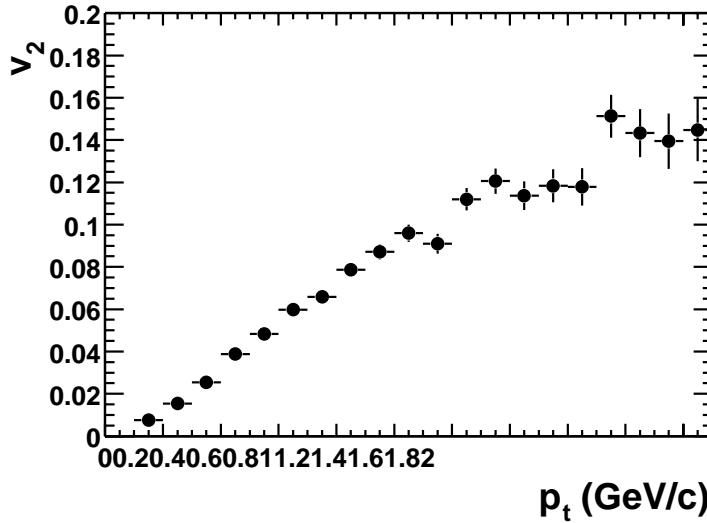


Figure 21. v_2 as a function of p_\perp , as measured by STAR in $\sqrt{s_{NN}} = 130$ GeV Au-Au collisions.

The differential anisotropic flow is a function of η and p_\perp . Figure 21 shows v_2 for charged particles as a function of p_\perp for a minimum bias event sample. Mathematically, the v_2 value at $p_\perp=0$, as well as its first derivative, must be zero, but it is interesting that v_2 appears to rise almost linearly with p_\perp starting from relatively low values of p_\perp . This is consistent with a stronger “in-plane” hydrodynamic expansion of the system than the average radial expansion.

Comparing to estimates based on transport cascade models, one finds that elliptic flow is under predicted by a factor of more than 2. Hydrodynamic calculations [32] for RHIC energies over predict elliptic flow by about 20-50%. This is just the reverse of the situation at the SPS where cascade models gave a reasonable description of the data and hydrodynamic calculations were more than a factor of two too high. Also in contrast to lower collision energies, the observed shape of the centrality dependence of the elliptic flow is similar to hydrodynamic calculations and thus consistent with significant thermalization which is one of the most striking results from the initial round of RHIC results.

6.3. TWO-PARTICLE INTERFEROMETRY (HBT)

The study of small relative momentum correlations, a technique also known as HBT [33] interferometry, is one of the most powerful tools to study complicated space-time dynamics of heavy ion collisions [34]. It provides crucial information which helps to improve our understanding of the reaction mechanisms and to constrain theoretical models of the heavy ion collisions. Interpretation of the extracted HBT parameters in terms of source sizes and lifetime is more or less straightforward for the case of chaotic static sources. In the case of expanding sources with strong space-momentum correlations (due to flow, etc.) the situation is more difficult, but the concept of length of homogeneity [35] provides a useful framework for the interpretation of data.

The dependence of the pion-emitting source parameters on the transverse momentum of the particle pairs (K_T) and on centrality can in principle be measured by all RHIC experiments with high statistics. For more detailed analysis as for example event-by-event HBT, HBT radii versus reaction plane, and the correlation of HBT results with other observables can only be performed by STAR due to its large acceptance and azimuthal coverage. These studies, however, are still in progress and it is by far too early to discuss them here. In the following we show results from the STAR experiment [36] that performed a multi-dimensional analysis using the standard Pratt-Bertsch decomposition [37] into outward, sideward, and longitudinal momentum differences and radius parameters. The data are analyzed in the longitudinally co-moving source frame, in which the total longitudinal momentum of the pair (collinear with the colliding beams) is zero.

As expected, larger sizes of the pion-emitting source are found for the more central (*i.e.* decreasing impact parameter) events, which in turn have higher pion multiplicities. This source size is observed to decrease with increasing transverse momentum of the pion pair. This dependence is similar to what has been observed at lower energies and is understood to be an effect of collective transverse flow. Shown in Figure 22 is the coherence parameter λ and the radius parameters R_{out} , R_{side} , and R_{long} obtained in the analysis. Also shown are values of these parameters extracted from similar analyses at lower energies. All analyses are for low transverse momentum (~ 170 MeV/ c) negative pion pairs at mid-rapidity for central collisions of Au + Au or Pb + Pb. From Figure 22 the values of λ , R_{out} , R_{side} , and R_{long} extend smoothly from the dependence at lower energies and do not reflect significant changes in the source from those observed at the CERN SPS energy. One of the biggest surprises is that the anomalously large source sizes or source lifetimes predicted for a long-lived mixed phase [38] have not been observed in this study. Preliminary results of the HBT analysis by the PHENIX Collaboration [39] agree with the STAR results within error bars.

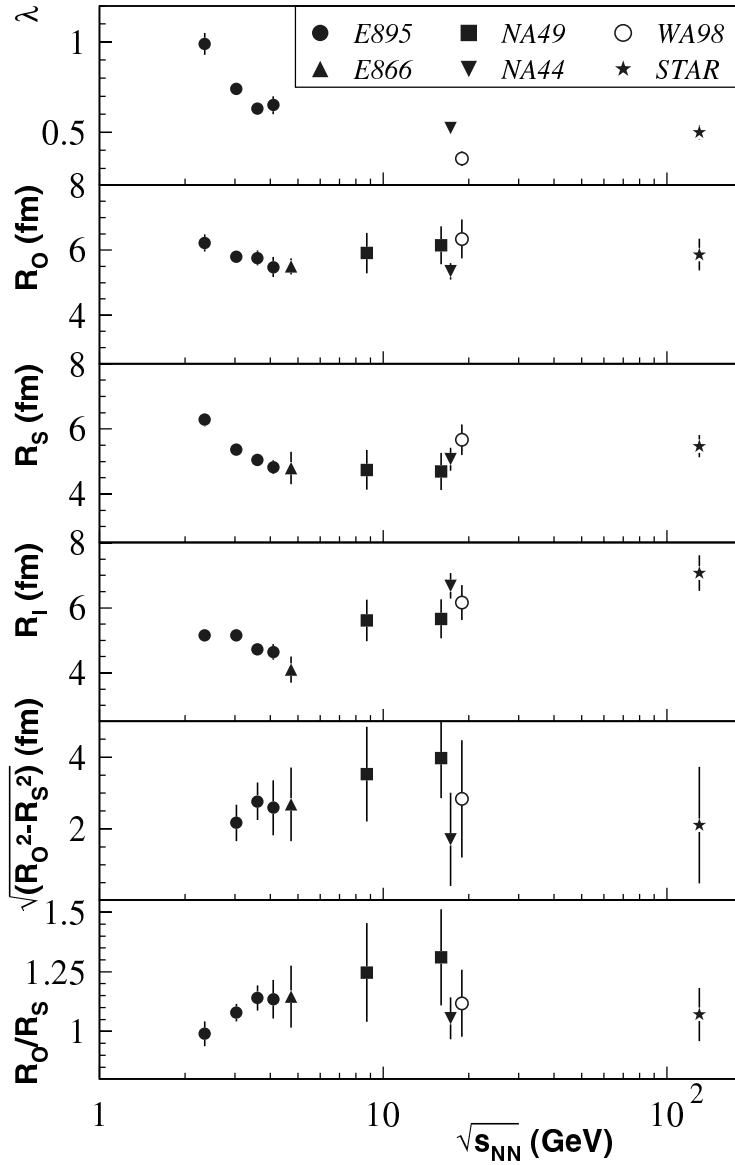


Figure 22. Compilation of results on two-particle correlation (HBT) parameters from measurements using central collisions of Au + Au at the BNL-AGS, Pb + Pb at the CERN-SPS and Au + Au data from the STAR experiment at RHIC. Plotted are the coherence parameter λ , R_{out} , R_{side} , and $R_{longitudinal}$.

One of the big puzzles, however, is the magnitude and the transverse momentum (K_T) dependence of the ratio of R_{out}/R_{side} which contradicts *all* model predictions [38, 40]. These model calculations predict the ratio to be greater than unity due to system lifetime effects which cause R_{out} to be larger than R_{side} . They also predict that the ratio increases with K_T . Such an increase seems to be a generic feature of the models based on the Bjorken-type, boost-invariant expansion scenario. Hence, it was surprising to see that the experimentally observed ratio is less than unity and is decreasing as a function of K_T . Currently, it is far from clear what kind of scenario can lead to such a puzzling K_T dependence.

6.4. HARD PROCESS PROBES OF THE PLASMA

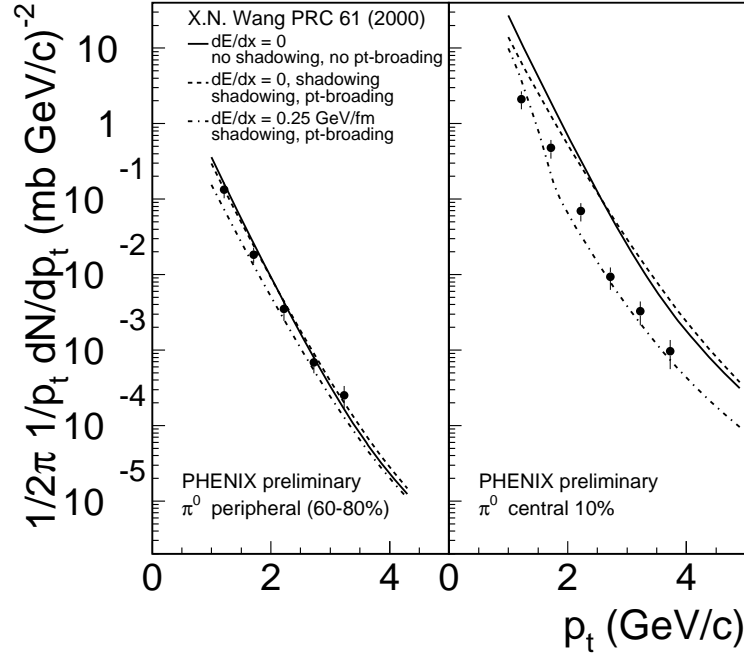


Figure 23. Preliminary PHENIX invariant multiplicity of identified π^0 as a function of transverse momentum are shown for peripheral and central collisions. Comparison with theoretical calculations with and without parton energy loss are also shown.

Jet processes and their associated hadronic fragmentation provide one of the most exciting probes of the color deconfined plasma. The PHENIX experiment has measured the distribution of identified π^0 for both central and peripheral Au-Au collisions as shown in Figure 23 [41]. The peripheral results appear to be in good agreement within systematic errors of an extrapolation from pp collisions scaled up by the number of binary collisions

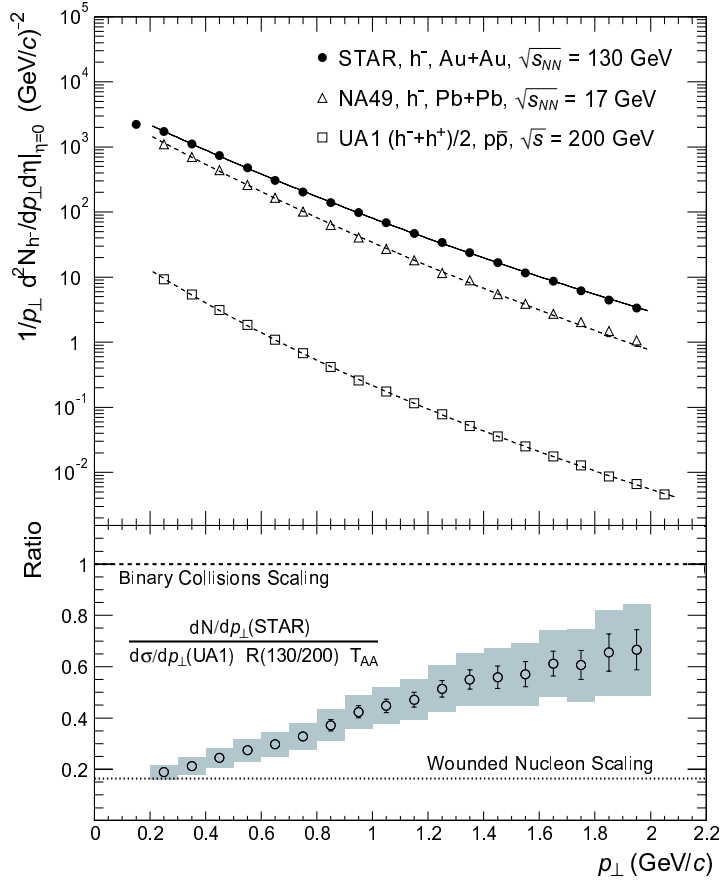


Figure 24. Invariant multiplicity of charged hadrons as a function of transverse momentum (top). Ratio of unidentified charge hadrons per calculated binary collision from Au + Au central collisions to those from $p + p(\bar{p})$ collisions extrapolated to $\sqrt{s_{NN}} = 130$ GeV as a function of transverse momentum (bottom).

expected in this centrality class. However, the central collision results show a significant suppression in the π^0 yield relative to this point like scaling expected for large momentum transfer parton-parton interactions. If the created fireball in RHIC collisions is transparent to quark jets, then we expect the yield of high p_{\perp} hadrons to obey point-like scaling and equal the pp (or equivalently $p\bar{p}$) distribution scaled up by the number of binary NN collisions, or equivalently by the nuclear thickness function T_{AA} . This is not what is observed. A more sophisticated calculation [42] yields the same qualitative conclusion.

The STAR experiment has recently submitted for publication [43] the p_{\perp} spectra for unidentified negatively charged hadrons in central Au + Au collisions as shown in Figure 24. Also shown are the equivalent spectra from

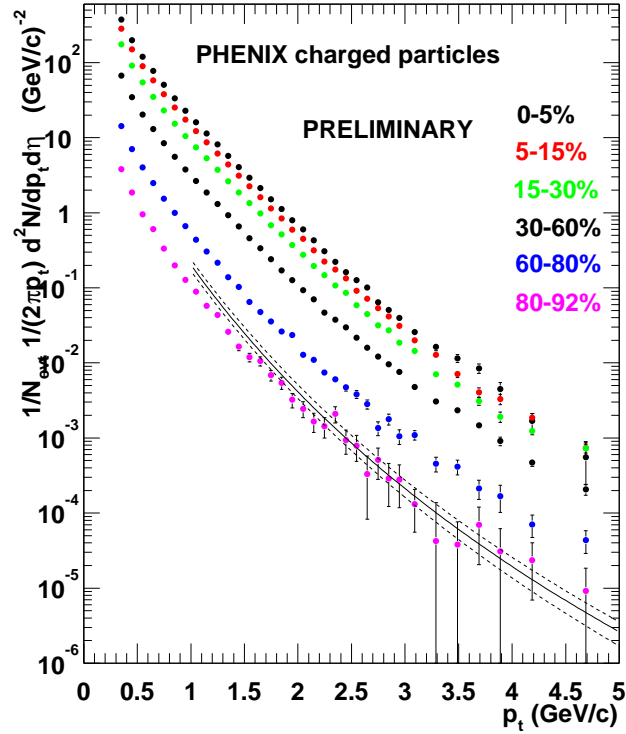


Figure 25. PHENIX preliminary results for unidentified charged hadron invariant multiplicity as a function of transverse momentum.

experiment NA49 at the CERN-SPS at $\sqrt{s} = 17$ GeV and from UA1 in $p\bar{p}$ at $\sqrt{s_{NN}} = 200$ GeV. The STAR spectra is then divided by the spectra from $p\bar{p}$ scaled by the number of binary collisions, and the result is shown in the lower panel of Fig 24. At low transverse momentum the particle production is dominated by soft interactions which scale with the number of wounded nucleons as indicated by the line at 0.2. The rise from 0.2 as a function of p_{\perp} certainly has a large contribution from hydrodynamic flow that will push particles to higher transverse momentum in central Au-Au collisions.

The PHENIX experiment has shown preliminary results extending out further in transverse momentum. Preliminary results for six centrality classes are shown from PHENIX in Fig 25. STAR also has preliminary results for central collisions extending out to $p_{\perp} > 5$ GeV that are in reasonable agreement with the PHENIX results. If one takes the ratio of the central spectra to the unidentified spectra in pp collisions scaled up by the number of binary collisions one gets a ratio R_{AA} as shown in Fig 26. It needs to be noted that there is no pp data at $\sqrt{s_{NN}} = 130$ GeV and thus an extrapolation to

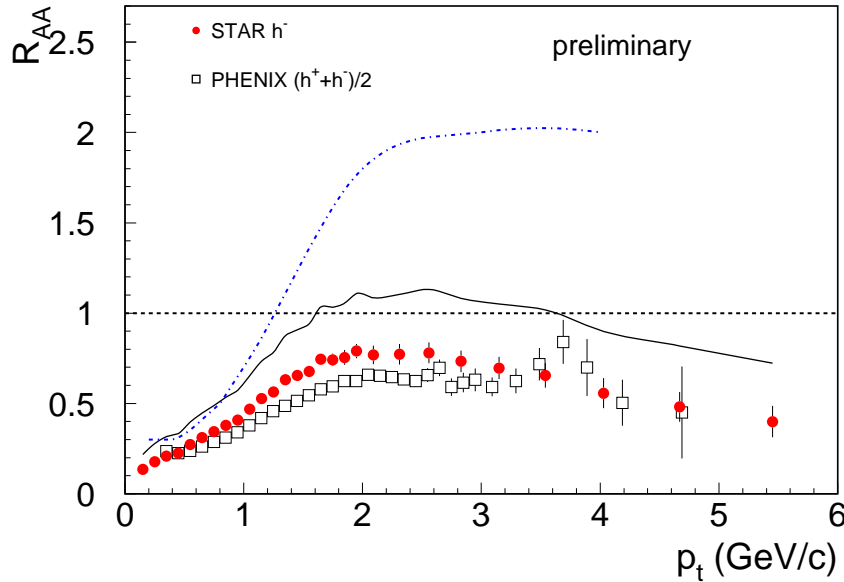


Figure 26. Ratio of unidentified charge hadrons per calculated binary collision from Au + Au central collisions to those from p + p(\bar{p}) collisions (extrapolated to $\sqrt{s_{NN}} = 130$ GeV) as a function of transverse momentum (GeV). The solid line is the systematic error band on the ratio. The dashed line is the average result from experiments at the lower energy CERN-SPS.

that energy is done to calculate R_{AA} . This extrapolation is included in the systematic error band, and should be reduced when both experiments measure the spectra in pp in Run II.

There are many important physics points to understand in these results. The ratio appears to stay below one, although that is a marginal conclusion with the present systematic errors. However, this is certainly in qualitative agreement with a parton energy loss scenario, as also seen in the observed suppression in the PHENIX π^0 spectra. In contrast, the CERN-SPS results show an enhancement that has been attributed to the Cronin effect, or initial state parton scattering that gives a k_T kick to the final transverse momentum distribution. This expected enhancement makes the suppression seen at RHIC all the more striking.

There are a number of open questions that must be considered before drawing any conclusions. The most basic is that these p_\perp values are low relative to where one might have confidence in the applicability of perturbative QCD calculations. In addition, the separation between soft and hard scale physics is blurred in this p_\perp range, and in fact the CERN-SPS ratio R_{AA} has also been explained in terms of hydrodynamic boosting of the soft physics to higher p_\perp . The preliminary results from PHENIX on the ratios of $\pi/K/p(\bar{p})$ in the middle of this p_\perp range look more like soft physics than a parton frag-

mentation function in vacuum. One additional point of concern is that these models of energy loss assume that the parton exits the collision region before finally fragmenting into a jet of forward hadrons. Thus the final hadronization takes place in vacuum. In the p_{\perp} range of these early measurements, that conclusion is not so clear. The parton is traveling through the medium with various k_T scatters, and if it hadronizes inside a bath of other particles, the leading hadrons may be slowed down by inelastic collisions with co-moving pions. Lastly, the point-like scaling is known to be violated due to the nuclear shadowing of parton distribution functions. These nuclear modifications are known to reduce the pdf for quarks of order 20% for $x \approx 10^{-2}$; however, the shadowing for gluons is not currently measured. The calculations of [42] have included modeling of this shadowing, but must be viewed with caution at this time. These points need further theoretical investigation. In addition, as will be discussed in the next section, many of these concerns are reduced when the measurements extend to much higher transverse momentum.

7. Future Measurements

In the following chapter, we discuss a few select topics within our areas of interest that have exciting results expected in the near future.

7.1. CHARM AND BOTTOM

The measurement of open charm and bottom in relativistic heavy ion collisions is both an extreme experimental challenge and rich with physics information. First, the measurement of quarkonium states such as the J/ψ require a comparison measure of the original $c\bar{c}$ production to determine the effect of color screening. Also, the total charm production is sensitive to the initial gluon density in the incoming nuclei and is thus sensitive to any shadowing of the gluon distribution function and may even comment on the possible color glass condensate postulated to describe the phase space saturated gluon distributions in the highly Lorentz contracted nuclei. Lastly, recent predictions of charm quark energy loss in traversing a hot partonic medium have generated much interest. Now for the difficult part. The best way to measure charm via D mesons is either via direct reconstruction from its $\pi + K$ decay mode or via the semi-leptonic decay $K + e + \nu_e$. The combinatoric background in the purely hadronic channel are close to overwhelming and the semi-leptonic decay cannot be completely reconstructed. In particle physics experiments measuring the decay products with a few micron displaced vertex from the collision vertex allows for a dramatic reduction in the combinatoric background. However, the level of silicon detector technology was not advanced enough for this very high multiplicity environment at the time of the RHIC

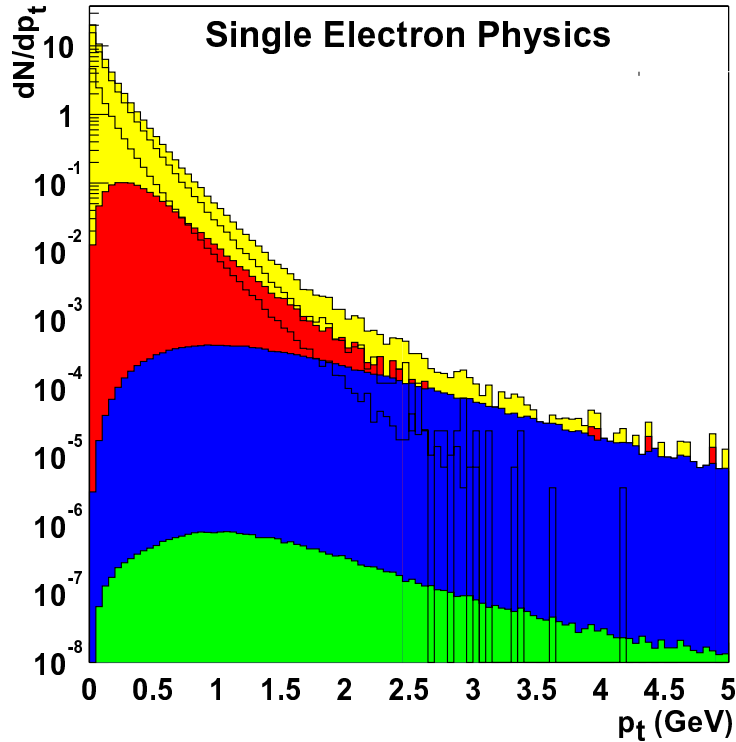


Figure 27. Simulation of the transverse momentum spectrum for mid-rapidity single electrons and positrons. The top curve is the sum of all contributions, the two lower curves are from Dalitz decays and photon conversions. The subsequent three grey shaded areas are from charm D mesons, beauty B mesons, and Drell-Yan.

detector designs. This is now being discussed as a possible upgrade to the experiments.

One promising way of determining the charm production is through the measurement of single electrons. Shown in Figure 27 is a simulation of single electrons as a function of transverse momentum. The top curve in the sum of all contributions. The next two curves that dominate the spectra at low $p_{\perp} < 1.0$ GeV and from the Dalitz decays of pions and η and from photon conversions. The next two contributions are from charm D meson and beauty B meson decays. Charm yields $\approx 50\%$ of the counts at $p_{\perp} = 1$ GeV, and beauty yields $> 50\%$ of the counts above $p_{\perp} > 3.5$ GeV. The lowest curve is the contribution from Drell-Yan which never has a major contribution to the single electrons.

PHENIX has made a preliminary measurement of the single electron transverse momentum spectra from the limited statistics in Run I as shown in Figure 28. The analysis of these results is proceeding and implications on charm production are forthcoming.

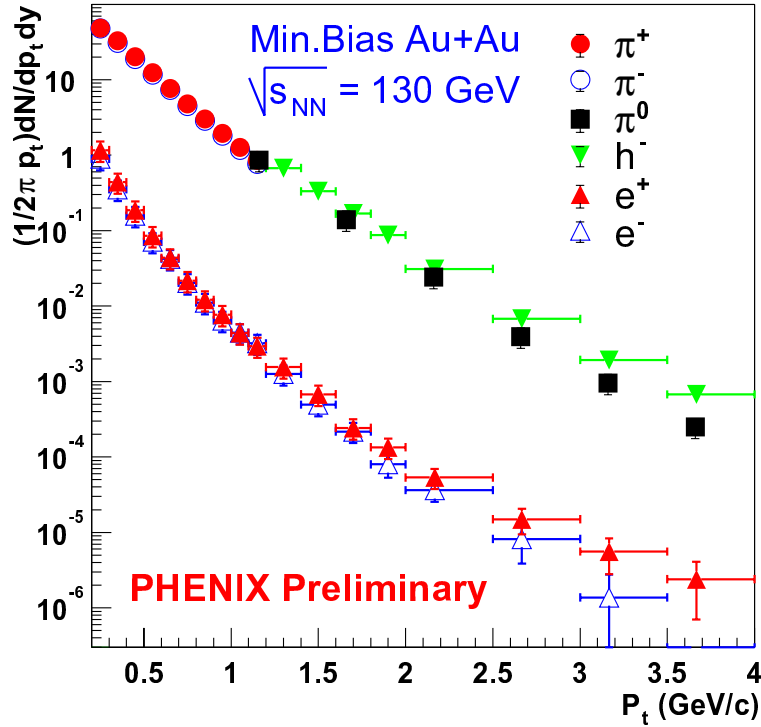


Figure 28. PHENIX preliminary results for unidentified charged hadron invariant multiplicity as a function of transverse momentum.

Additional handles on heavy flavor production can be had with the measurement of correlated leptons. For example, electron-muon pairs at large relative momentum (Q^2 or M_{inv}) have a substantial contribution from $c\bar{c}$ and $b\bar{b}$ pairs. For example, the $c\bar{c}$ can fragment into $D\bar{D}$ followed by the decays $D \rightarrow K + e + \nu_e$ and $\bar{D} \rightarrow K + \mu + \nu_\mu$. Although the initial Q^2 of the $c\bar{c}$ pair is significantly modified when measured as a Q^2 of the $e\mu$ pair, there is enough information to attempt to extract a total charm cross section and maybe something about the initial Q^2 of the $c\bar{c}$. This measurement has the advantage over e^+e^- and $\mu^+\mu^-$ pairs in that $e\mu$ pairs are free from Drell-Yan and thermal contributions.

One of us (J.N.) has used PYTHIA 6.0 to estimate the rate of $e\mu$ pairs into the PHENIX acceptance (Central arms for the electron and South muon arm only for the μ). PYTHIA has been run with a charm quark mass of 1.5 GeV/ c^2 and $\langle k_T \rangle = 1.5$ GeV/ c .

We show in Figure 29 the distribution of Q^2 for all $c\bar{c}$, $D\bar{D}$, $e\mu$ and $e\mu$ pairs accepted by PHENIX. One can see that the charm mesons carry most of the information from the $c\bar{c}$ pair. For the $e\mu$ pair the correlation with the $c\bar{c}$ pair Q^2 is substantially washed out and of much lower slope since the kaon in

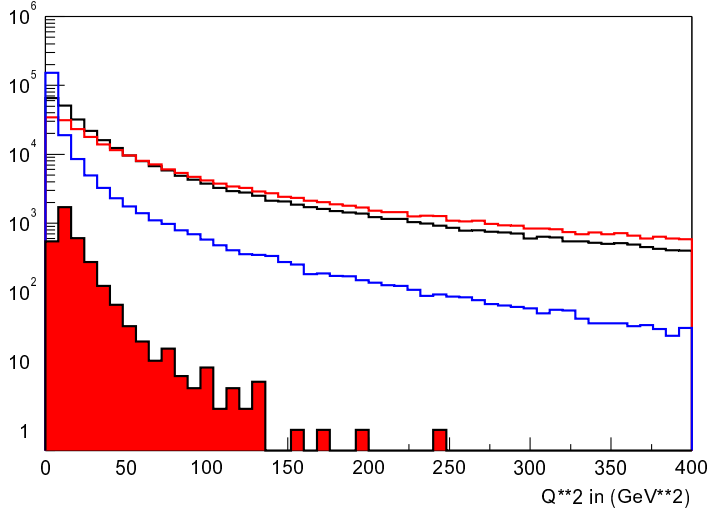


Figure 29. Q^2 in GeV^2 for $c\bar{c}$ (black line), $D\bar{D}$ (red line), $e\mu$ (blue line), and $e\mu$ accepted by PHENIX (red fill). The vertical scale is arbitrary between the different curves.

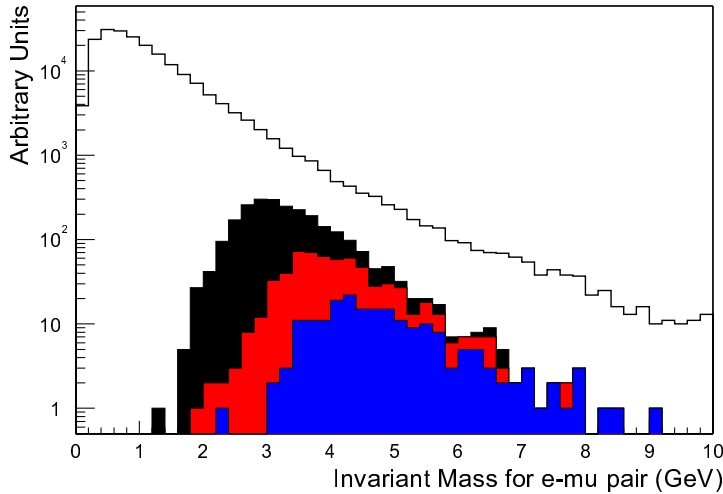


Figure 30. $e\mu$ Invariant Mass Distribution in GeV. Shown are all $e\mu$ pairs (black line), $e\mu$ pairs with the muon penetrating to gap 5 and $E(\text{electron}) > 1.0$ GeV (black fill), with $E(\text{electron}) > 1.5$ GeV (red fill), $E(\text{electron}) > 2.0$ GeV (blue fill).

the D decay takes away a large fraction of the original charm momentum that is not measured. It should be noted that the modeling of the fragmentation of the charm quark will be a source of systematic error, whereas the blurring of the Q^2 from the $e\mu$ decay kinematics can be modeled exactly.

We show the invariant mass distribution of the $e\mu$ pairs into the PHENIX acceptance in Figure 30. Also shows are three mass distribution with electron

energy cuts of 1.0, 1.5, and 2.0 GeV. The cut on the electron energy is strongly correlated with the invariant mass selection on the $e\mu$ pair. Since lower masses (in particular $m < 4.0$ GeV) are thought to have large background contamination, the loss of these pairs with higher electron energy threshold are not as worrisome as they might otherwise be. It may be necessary to use the electron energy in order to selectively trigger on these events.

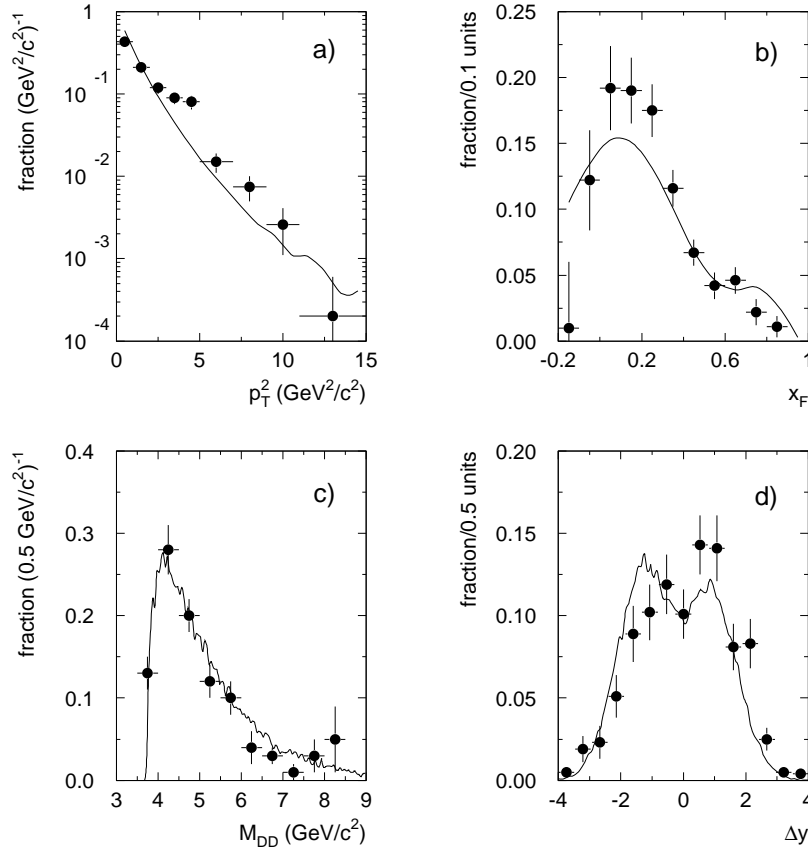


Figure 31. $D\bar{D}$ data from $\pi^- - Cu$ collisions at $\sqrt{s} = 26$ GeV. In particular, panel d) shows the $D\bar{D}$ rapidity difference $\Delta y = y_D - y_{\bar{D}}$.

Measuring charm by this method requires an accurate model of the $c\bar{c}$ distribution in Q^2 , and the corresponding Δy (rapidity gap) and Δp_{\perp} . In Figure 31 PYTHIA is compared to some of the only data on the rapidity gap between D and \bar{D} mesons [44]. The agreement is not bad, but it the comparison is not a great confidence builder in the ability to model and then test by data checking this input. More experimental data are needed and theoretical work to model charm production.

In order to draw a full picture of charm production, multiple measurements must be done in the single lepton (electrons and muons) and correlated

leptons (electron pairs, muon pairs, and electron-muon pairs). It would be extremely useful for theorists interested in total charm or beauty production, and also high p_{\perp} energy loss of heavy flavor partons, to make some predictions for the leptonic signatures that will be measured in the next year. Future upgrades to the detectors for tagging displaced vertices from D meson decays are probably more than five years away.

7.2. QUARKONIA (PHENIX)

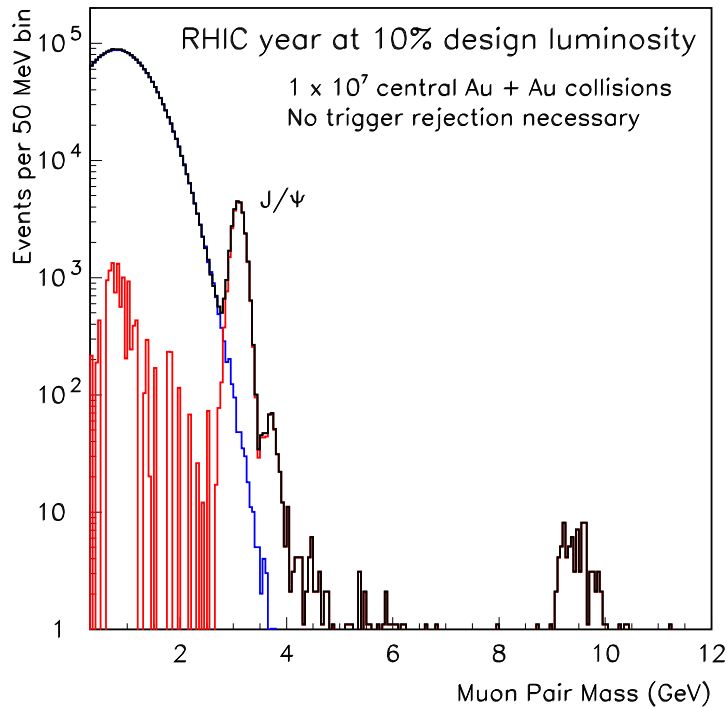


Figure 32. Simulation study of dimuons in the PHENIX muon spectrometers.

There are no early measurement results on quarkonia J/ψ states from Run I due to the low luminosity and short running period. The PHENIX experiment will make a measurement of J/ψ and other states in both the muon and electron channels in Run II. PHENIX has a large acceptance in x_F and p_{\perp} that will be crucial to constraint models of color screening absorption and test theories with re-coalescence at the hadronization phase. Shown in Figure 32 is a simulation of the type of measurement that could be made in the PHENIX muons arms with 37 weeks at 10% of design luminosity, or equivalently in less than four weeks with the luminosity averaging the the RHIC design specification. The first measurements are being made now in Run II, and high statistics should be available in Run III.

7.3. QUARKONIA (STAR)

The STAR detector system is unique among the RHIC experiments in its capabilities to simultaneously measure many experimental observables on a event-by-event basis such as energy-density, entropy, baryochemical potential, strangeness content, temperature, and flow. The measurement of J/Ψ production as a function of these quantities allows the study of the suppression mechanism in great detail. This advantage becomes immediately apparent when it comes to the study of the *onset* of the anomalous suppression which reflects the point where the system reaches critical conditions and, at least partially, undergoes a phase transition. Thus, the correlation of the $c\bar{c}$ break-up with the many single-event variables provides a new promising analysis tool.

The golden J/Ψ decay mode for STAR is $J/\Psi \rightarrow e^+e^-$. Prima facie this poses a problem since the STAR detector has been designed to focus primarily on hadronic observables over a large phase-space and thus lacks two essential features of a dedicated lepton experiment: hadron-blind detectors and fast event recording rates. The two essential components which help to overcome these shortcomings are (i) the EMC barrel which allows to suppress hadrons to a level sufficient to achieve signal-to-background ratios around 1:3 or better, and (ii) a fast level-3 trigger which is designed to efficiently trigger on electron-positron pairs with a given invariant mass at rates in the order of 100 Hz, thus improving STARs bandwidth for recording J/Ψ decays by almost two orders of magnitude.

The geometric acceptance for the decay channel $J/\Psi \rightarrow e^+e^-$ in STAR is shown in Fig. 33. A J/Ψ is accepted if both electrons carry momenta $p > 1.5$ GeV/c and fall into the EMC acceptance. Both requirements imply that the electron tracks cross all layers of inner tracking detectors (SVT+SSD) and all TPC padrows. This ensures maximum momentum and dE/dx resolution and therefore maximum additional electron identification from detectors other than the EMC. As is depicted in the left plot, the full coverage of the EMC $|\eta| < 1$ ensures relatively high efficiencies ($\sim 8\%$) at very low p_\perp . At these low values the two leptons run essentially back-to-back, a decay topology that requires symmetric coverage around $y = 0$. This region of phasespace is of great interest since here the J/Ψ remains longest in the hot dense medium and its breakup probability is maximal. Up to $p_\perp = 1$ GeV/c the acceptance then drops significantly since, still at large opening angles, it becomes more likely to loose one electron because it either carries too low momentum and/or falls outside our acceptance. At larger p_\perp the acceptance raises dramatically due to the decreasing opening angle of the pair and the higher average momenta of the electrons. However, the J/Ψ cross-section drops exponentially towards larger p_\perp resulting in little net benefit in terms

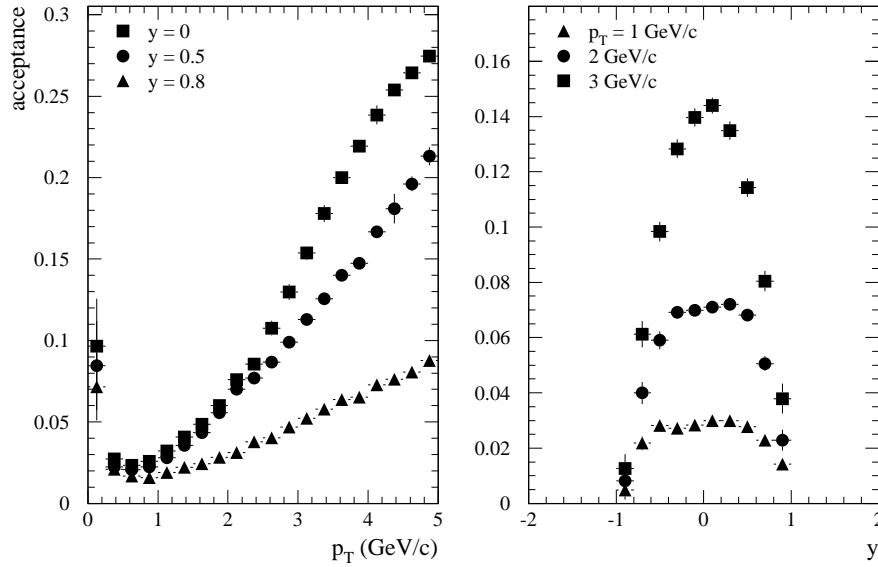


Figure 33. Geometrical acceptance for $J/\Psi \rightarrow e^+e^-$ in the STAR experiment. The left plot shows the acceptance as a function of p_\perp for various rapidities y , right one as a function of rapidity for various p_\perp slices.

of total yields. In this region the acceptance scales approximately *linear* with the EMC coverage while at lower p_\perp it scales almost *quadratically*.

The dominant background source is the 'combinatorial background' due to pions misidentified as electrons. Other sources as electrons from π^0 - and η -Dalitz decays, photo-conversions, and decays of light vector-mesons (ρ , ϕ) turned out to be neglectable, since (i) their average p_\perp is too low and (ii) their rate is small compared to the abundance of misidentified hadrons. In addition, most electrons from photo-conversion can easily be rejected by requiring that all tracks point back to the primary event vertex.

The most crucial factor in the overall background rejection is the hadron rejection power (e/h) of the EMC. However, for $p < 2$ GeV/c, a region where the hadron rejection capabilities of the EMC are degraded, the combined dE/dx information of SVT and TPC helps to augment the S/B ratio considerably. It is important to note, that the hadron rejection enters quadratically into the background.

The magnitude of the background depends strongly on the momentum cut applied to the electron candidates. In order to access the low- p_\perp J/Ψ region STAR has chosen $m_{J/\psi}/2 \simeq 1.5$ GeV/c as the lowest value to study. The higher the cut the better the e/h rejection from the EMC and the lower the charged pion yield.

Table I. Current estimates on J/Ψ yields, signal-to-background ratio, and statistical significance of the signal in the STAR experiment.

cut	J/Ψ -yield	S/B	σ after 10^7 sec	σ after 10^6 sec
$p_e > 1.5$ GeV/ c	40 k	1:3	76	24
$p_e > 2.0$ GeV/ c	10 k	3:1	77	24

Before any measurement can be addressed it is important to estimate the achievable yields and the statistical significance of the signal under realistic assumptions. Table 7.3 summarizes the resulting yields, the signal-to-background ratio, and the statistical significance after 10^7 and 10^6 sec. Note, that a nominal RHIC run has 10^7 sec. Here one assumes 100% level-3 trigger efficiency running at the design rate of 100 Hz, and full EMC coverage including pre-shower detectors. The estimate includes the reconstruction efficiencies of the various detectors. Known cross-section from elementary collisions were used to extrapolate to Au+Au at $\sqrt{s_{NN}} = 200$ GeV. Two different sets of cuts on the electron momenta are shown in order to demonstrate its effect on the S/B ratio. Interestingly, the higher S/B ratio for the larger p_{\perp} cut balances the decreased signal strength, thus resulting in the same statistical significance for both cases.

For the actual measurement one has to study J/Ψ production not only in the most central collisions, but has to vary the centrality and possibly the colliding systems. Although the J/Ψ yield will decrease for semi-central and peripheral collisions the signal-to-background ratio will decrease even stronger (almost quadratically) which will ease the extraction of the signal significantly.

8. Summary and Conclusions

The workshop was a wonderful forum for learning and exchanging new ideas about the physics relevant at RHIC. There is lots of exciting physics in a field with much potential for discovery. We wish to thank the organizers and all the students for their active participation and thought provoking questions.

References

1. R. Hagedorn, Suppl. A. Nuovo Cimento VolIII, No.2 (1965) 150.
2. P. Braun-Munzinger, I. Heppe, and J. Stachel, Phys. Lett. B465 (1999) 15.
3. P. Braun-Munzinger *et al.*, Phys.Lett. B518 (2001) 41-46.

4. T. Matsui and H. Satz, Phys. Lett. B178, 416 (1986).
5. R. Baier, Y.L. Dokshitzer, A.H. Mueller and D. Schiff, Phys. Rev. C58, 1706 (1998); hep-ph/9803473.
6. R. Baier, Y.L. Dokshitzer, A.H. Mueller, S. Peigne and D. Schiff, Nucl. Phys. B483, 291 (1997); hep-ph/9607355.
7. Conceptual Design Report for the Solenoidal Tracker At RHIC, The STAR Collaboration, PUB-5347 (1992); J.W. Harris *et al.*, Nucl. Phys. A 566, 277c (1994).
8. PHENIX Experiment at RHIC - Preliminary Conceptual Design Report, PHENIX Collaboration Report (1992).
9. Interim Design Report for the BRAHMS Experiment at RHIC, BNL Report (1994).
10. RHIC Letter of Intent to Study Very Low pt Phenomena at RHIC, PHOBOS Collaboration (1991).
11. Proposal on Spin Physics Using the RHIC Polarized Collider, RHIC Spin Collaboration (1992).
12. B.B. Back *et al.* (PHOBOS), Phys. Rev. Lett. 85, 3100 (2000); hep-ex/0007036.
13. K. Adcox *et al.* (PHENIX), Phys. Rev. Lett. 86, 3500 (2001); nucl-ex/0012008.
14. F. Videbaek *et al.* (BRAHMS), Proceedings to the 15th International Conference on Ultrarelativistic Nucleus-Nucleus Collisions 2001.
15. J. Harris *et al.* (STAR), Proceedings to the 15th International Conference on Ultrarelativistic Nucleus-Nucleus Collisions 2001.
16. B.B. Back *et al.* (PHOBOS); nucl-ex/0105011.
17. K.J. Eskola, K. Kajantie, and K. Tuominen, Phys. Lett. B497, 39 (2001); hep-ph/0009246.
18. X.N. Wang and M. Gyulassy, Phys. Rev. Lett. 86, 3496 (2001); nucl-th/0008014.
19. J.D. Bjorken, Phys. Rev. D, Vol. 27, page 140 (1983).
20. I.G. Bearden *et al.* (BRAHMS); nucl-ex/0106011.
21. K. Adcox *et al.* (PHENIX), Phys. Rev. Lett. 87, 052301 (2001); nucl-ex/0104015.
22. See contribution of J.-Y. Ollitrault in these proceedings.
23. H. Sorge, Phys. Lett. B402, 251 (1997).
24. J.-Y. Ollitrault, Phys. Rev. D 46, 229 (1992).
25. E877 Collaboration, J. Barrette *et al.*, Phys. Rev. C 55, 1420 (1997).
26. E895 Collaboration, C. Pinkenburg *et al.*, Phys. Lett. 83, 1295 (1999).
27. NA49 Collaboration, H. Appelshäuser *et al.*, Phys. Lett. 80, 4136 (1998).
28. A.M. Poskanzer and S.A. Voloshin for the NA49 Collaboration, Nucl. Phys. A661, 341c (1999).
29. WA98 Collaboration, M.M. Aggarwal *et al.*, Phys. Lett. B403, 390 (1997); M.M. Aggarwal *et al.*, Nucl. Phys. A638, 459 (1998).
30. STAR Collaboration, K.H. Ackermann *et al.*, Phys. Lett. 86, 402 (2001).
31. S.A. Voloshin and A.M. Poskanzer, Phys. Lett. B474, 27 (2000).
32. P.F. Kolb, J. Sollfrank, and U. Heinz, Phys. Rev. C 62, 054909 (2000).
33. R. Hanbury Brown and R.Q. Twiss, Phil. Mag. 45 (1954) 663.
34. U.A. Wiedemann and U. Heinz, Rhys. Rept. 319 (1999) 145.,
35. A. Makhlin and Y. Sinyukov, Z. Phys. C39 (1998) 69.
36. C. Adler *et al.*, Phys. Rev. Lett. 87, 082301 (2001).
37. S. Pratt, Phys. Rev. D 33, 1314 (1986); G. Bertsch, M. Gong and M. Tohyama, Phys. Rev. C37, 1896 (1988); and G. Bertsch, Nucl. Phys. A498, 151c (1989).
38. D. H. Rischke, Nucl. Phys. A610 (1996) 88c; D.H. Rischke and M. Gyulassy, Nucl. Phys. A608 (1996) 479.
39. S.C. Johnson, nucl-ex/0104020.
40. S. Soff, S.A. Bass and A. Dumitru, nucl-th/0012085.

41. W.A. Zajc *et al.* (PHENIX), Proceedings to the 15th International Conference on Ultrarelativistic Nucleus-Nucleus Collisions 2001; nucl-ex/0106001.
42. X.N. Wang, Phys. Rev. C61, 064910 (2000); nucl-th/9812021.
43. C. Adler *et al.* (STAR); nucl-ex/0106004.
44. P. Braun-Munzinger *et al.*, Eur. Phys. J. C1 (1998) 123-130; nucl-ex/9704011.

Address for Offprints:

KLUWER ACADEMIC PUBLISHERS PrePress Department,
P.O. Box 17, 3300 AA Dordrecht, The Netherlands
e-mail: TEXHELP@WKAP.NL
Fax: +31 78 6392500